# Heat-Transfer and Solidification Model of Continuous Slab Casting: CON1D

YA MENG and BRIAN G. THOMAS

A simple, but comprehensive model of heat transfer and solidification of the continuous casting of steel slabs is described, including phenomena in the mold and spray regions. The model includes a one-dimensional (1-D) transient finite-difference calculation of heat conduction within the solidifying steel shell coupled with two-dimensional (2-D) steady-state heat conduction within the mold wall. The model features a detailed treatment of the interfacial gap between the shell and mold, including mass and momentum balances on the solid and liquid interfacial slag layers, and the effect of oscillation marks. The model predicts the shell thickness, temperature distributions in the mold and shell, thickness of the resolidified and liquid powder layers, heat-flux profiles down the wide and narrow faces, mold water temperature rise, ideal taper of the mold walls, and other related phenomena. The important effect of the nonuniform distribution of superheat is incorporated using the results from previous three-dimensional (3-D) turbulent fluid-flow calculations within the liquid pool. The FORTRAN program CONID has a user-friendly interface and executes in less than 1 minute on a personal computer. Calibration of the model with several different experimental measurements on operating slab casters is presented along with several example applications. In particular, the model demonstrates that the increase in heat flux throughout the mold at higher casting speeds is caused by two combined effects: a thinner interfacial gap near the top of the mold and a thinner shell toward the bottom. This modeling tool can be applied to a wide range of practical problems in continuous casters.

## I. INTRODUCTION

HEAT transfer in the continuous slab-casting mold is governed by many complex phenomena. Figure 1 shows a schematic of some of these. Liquid metal flows into the mold cavity through a submerged entry nozzle and is directed by the angle and geometry of the nozzle ports.[1] The direction of the steel jet controls turbulent fluid flow in the liquid cavity, which affects delivery of superheat to the solid/liquid interface of the growing shell. The liquid steel solidifies against the four walls of the water-cooled copper mold, while it is continuously withdrawn downward at the casting speed.

Mold powder added to the free surface of the liquid steel melts and flows between the steel shell and the mold wall to act as a lubricant,[2] so long as it remains liquid. The resolidified mold powder, or "slag," adjacent to the mold wall cools and greatly increases in viscosity, thus acting like a solid. It is thicker near and just above the meniscus, where it is called the "slag rim." The slag cools rapidly against the mold wall, forming a thin solid glassy layer, which can devitrify to form a crystalline layer if its residence time in the mold is very long.[3] This relatively solid slag layer often remains stuck to the mold wall, although it is sometimes dragged intermittently downward at an average speed less than the casting speed.[4] Depending on its cooling rate, this slag layer may have a structure that is glassy, crystalline, or a combination of both.[5] So long as the steel shell remains above its crystallization temperature, a liquid slag layer will move downward, causing slag to be consumed at a rate balanced by the replenishment of bags of solid powder to the top surface. Still more slag is captured by the oscillation marks and other imperfections of the shell surface and carried downward at the casting speed.

These layers of mold slag comprise a large resistance to heat removal, although they provide uniformity relative to the alternative of an intermittent vapor gap found with oil casting of billets. Heat conduction across the slag depends on the thickness and conductivity of its layers, which, in turn, depends on their velocity profile, crystallization temperature,[6] viscosity, and state (glassy, crystalline, or liquid). The latter can be determined by the time-temperature-transformation (TTT) diagram measured for the slag, knowing the local cooling rate.[7,8,9] Slag conductivity depends mainly on the crystallinity of the slag layer and on the internal evolution of its dissolved gas to form bubbles.

Shrinkage of the steel shell away from the mold walls may generate contact resistances or air gaps, which act as a further resistance to heat flow, especially after the slag is completely solid and unable to flow into the gaps. The surface roughness depends on the tendency of the steel shell to "ripple" during solidification at the meniscus to form an uneven surface with deep oscillation marks. This depends on the oscillation practice, the slag-rim shape and properties, and the strength of the steel grade relative to the ferrostatic pressure, mold taper, and mold distortion. These interfacial resistances predominantly control the rate of heat flow in the process.

Finally, the flow of cooling water through vertical slots in the copper mold withdraws the heat and controls the temperature of the copper mold walls. If the "cold face" of the mold walls becomes too hot, boiling may occur, which causes variability in heat extraction and accompanying defects. Impurities in the water sometimes form scale deposits

YA MENG, Graduate Student, Department of Materials Science and Engineering, and BRIAN G. THOMAS, Professor, Department of Mechanical and Industrial Engineering, are with the University of Illinois at Urbana–Champaign, Urbana, IL 61801. Contact e-mail: bgthomas@uiuc.edu

Manuscript submitted August 27, 2002.

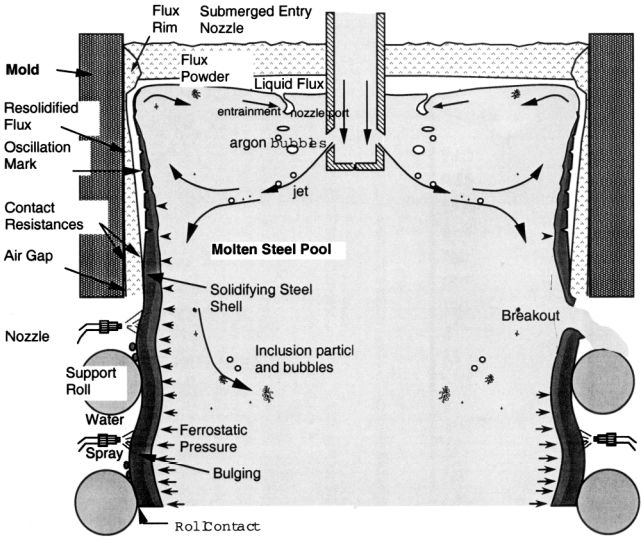


Fig. 1—Schematic of continuous casting process showing slag layers (not to scale).

on the mold cold face, which can significantly increase the mold temperature, especially near the meniscus where the mold is already hot. After exiting the mold, the steel shell moves between successive sets of alternating support rolls and spray nozzles in the spray zones. The accompanying heat extraction causes surface-temperature variations while the shell continues to solidify.

It is clear that many diverse phenomena simultaneously control the complex sequence of events which govern heat transfer in the continuous casting process. The present work was undertaken to develop a fast, simple, and flexible model to investigate these heat-transfer phenomena. In particular, the model features a detailed treatment of the interfacial gap in the mold, which is the most important thermal resistance. The model includes heat, mass, momentum and force balances on the slag layers in the interfacial gap.

This model is part of a larger comprehensive system of models of fluid flow, heat transfer, and mechanical behavior, which is being developed and applied to study the formation of defects in the continuous casting process. These other models are used to incorporate the effects of mold distortion,[10] the influence of fluid flow in the liquid pool on solidification of the shell,[11] and coupled thermal-stress analysis of the shell to find the reduction of heat transfer across the interface due to air-gap formation.[12]

This article first describes the formulation of this model, which has been implemented into a user-friendly FORTRAN program, CONID, on personal computers and UNIX workstations. Then, validation of the model with analytical solutions and calibration with example plant measurements are presented. Finally, the effect of casting speed on mold heat transfer is investigated as one example of the many applications of this useful modeling tool.

## II. PREVIOUS WORK

Many mathematical models have been developed of the continuous casting process, which are partly summarized in previous literature reviews.[13,14,15] Many continuous-casting models are very sophisticated (even requiring supercomputers to run), so are infeasible for use in an operating environment. The earliest solidification models used one-dimensional (1-D) finite-difference methods to calculate the temperature field and growth profile of the continuously cast steel shell.[16,17] Many industrial models followed.[18,19] These models first found application in the successful prediction of metallurgical length, which is also easily done by solving the following simple empirical relationship for distance ($z$) with the shell thickness ($S$) set to half the section thickness:

$$S = K\sqrt{z/V_c} \qquad [1]$$

where $K$ is found from evaluation of breakout shells and computations. Such models found further application in troubleshooting the location down the caster of hot-tear cracks initiating near the solidification front[20] and in the optimization of cooling practice below the mold to avoid subsurface longitudinal cracks due to surface reheating.[21]

Since then, many advanced models have been developed to simulate further phenomena such as thermal stress and crack-related defects[12,22,23] or turbulent fluid flow[24–28] coupled together with solidification. For example, a two-dimensional (2-D) transient, stepwise coupled elasto-viscoplastic finite-element model tracks the behavior of a transverse slice through a continuously cast rectangular strand as it moves down through the mold at casting speed.[12] This model is suited for simulating longitudinal phenomena such as taper design,[29] longitudinal cracks,[30] and surface depressions.[31] Other casters have been modeled using three-dimensional (3-D) coupled fluid flow–solidification models[27] based on control-volume or finite-difference approaches, at the expense of greater computation time and memory.

To study the temperature distribution and/or distortion of the mold, 3-D finite-element thermal-stress models have been applied.[10,32] These models have been crucial in determining the axial heat-flux profile based on measured temperatures in the mold walls.[20,32,33] This procedure is sometimes automated with inverse heat-conduction models.[20]

One of the greatest resistance to heat transfer from the liquid steel to the mold cooling water is the interface between the mold and shell. Heat transfer across this interface is controlled by the thickness and thermal properties of the materials that fill the gap. Despite its known importance, most previous mathematical models characterize the interface as a boundary condition for a model of either the shell or the mold alone. Even models of both usually use a simplified treatment of the gap.[34,35,36]

A few models have considered more-detailed treatment of the resolidified powder layers in the gap and can calculate slag-layer thicknesses,[37,38] the slag velocity profile along the film thickness,[38,39] and interface friction.[37,38,39] Common oversimplifications include neglecting the solid slag layer,[40] assuming a constant slag-layer thickness,[39] or assuming a constant slag viscosity.[41,42] The highly temperature-dependent slag viscosity has been modeled with a simple inverse function of temperature[38] or with an Arrhenius equation,[37,39,43] by fitting the low viscosities (usually less than 10 Pa·s) measured at high temperatures and then extrapolating to lower temperatures. Even the best interface models generally oversimplify the shell and/or the mold.

Thus, there is a need for a comprehensive model of the shell, mold, and gap, which is fast and easy to run, for use in both research and steel plant environments.

## III. MODEL FORMULATION

The model in this work computes 1-D transient heat flow through the solidifying steel shell, coupled with 2-D steady-state heat conduction within the mold wall. Superheat from the liquid steel was incorporated as a heat source at the steel solid/liquid interface. The model features a detailed treatment of the interfacial gap, including mass and momentum balances on the liquid and solid slag layers, friction between the slag and mold, and slag-layer fracture. The model simulates axial ($z$) behavior down a chosen position on the mold perimeter. Wide-face, narrow-face, and even corner simulations can, thus, be conducted separately.

### A. *Superheat Delivery*

Before it can solidify, the steel must first cool from its initial pour temperature to the liquidus temperature. Due to turbulent convection in the liquid pool, this "superheat" contained in the liquid is not distributed uniformly. A small database of results from a 3-D fluid-flow model[11] is used to determine the heat flux ($q_{sh}$) delivered to the solid/liquid interface due to the superheat dissipation, as a function of distance below the meniscus. The initial condition of the liquid steel at the meniscus is then simply the liquidus temperature.

Previous work[11] found that this "superheat flux" varies linearly with the superheat temperature difference and also is almost directly proportional to casting speed. The superheat-flux ($q_{sh}$) function in the closest database case is adjusted to correspond with the current superheat temperature difference ($\Delta T_{sup}$) and casting speed ($V_c$) as follows:

$$q_{sh} = q^0_{sh} \frac{\Delta T_{sup}}{\Delta T^0_{sup}} \frac{V_c}{V^0_c} \qquad [2]$$

where $q^0_{sh}$ is the superheat-flux profile from the database case, with conditions of a superheat temperature difference of $\Delta T^0_{sup}$ and a casting speed of $V^0_c$. Further adjustments are made to translate the heat-flux peak to account for differences in nozzle configuration between the current conditions and the database. Examples of the superheat-flux function are included in Figure 2, which represents results for a typical bifurcated, downward-directed nozzle. The influence of this function is insignificant to shell growth over most of the wide face, where the superheat flux is small and contact with the mold is good.

### B. *Heat Conduction in the Solidifying Steel Shell*

The temperature in the thin solidifying steel shell is governed by the 1-D transient heat-conduction equation, which becomes the following on applying the chain rule to the temperature-dependent conductivity:

$$\rho_{steel}\, Cp^*_{steel} \frac{\partial T}{\partial t} = k_{steel} \frac{\partial^2 T}{\partial x^2} + \frac{\partial k_{steel}}{\partial T} \left( \frac{\partial T}{\partial x} \right)^2 \qquad [3]$$

Temperature-dependent properties are given in Appendix D.[44,45] Both the sensible and latent heat of steel are included in the effective specific heat ($Cp^*_{steel}$), explained in Section IV–C.

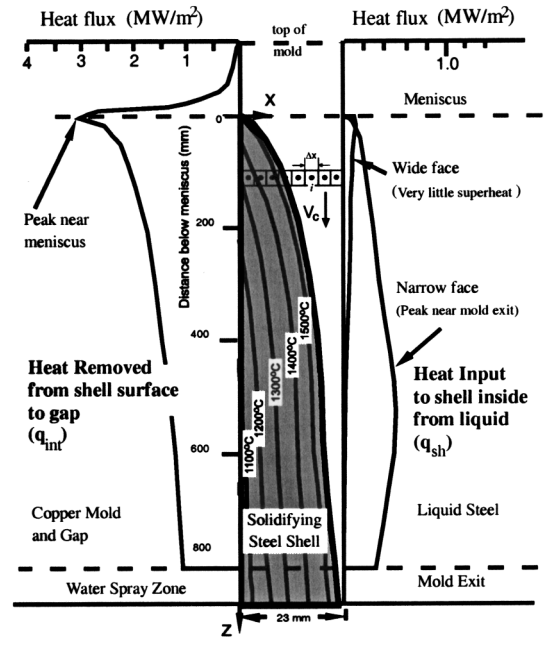


Fig. 2—Model of solidifying steel shell domain showing typical isotherms and heat flux conditions.

This equation assumes that axial ($z$) heat conduction is negligible in the steel, which is reasonable past the top 10 mm, due to the large advection component as indicated by the large Péclet number: $\text{Pe} = V_c Z_{mold} \rho_{steel} Cp_{steel} / k_{steel} = 0.0167 \times 0.81 \times 7400 \times 670/30 = 2236$. The simulation domain for this portion of the model is a slice through the liquid steel and solid shell, which moves downward at the casting speed, as pictured in Figures 2 and A-1, together with typical interface conditions. At the internal solid/liquid steel interface, the superheat flux delivered from the turbulent liquid pool (Section III–A) is imposed as a source term. From the external surface of the shell, interfacial heat flux ($q_{int}$) is lost to the gap, which depends on the mold and slag-layer computations, described in the following two sections. Appendix A provides the explicit finite-difference solution of Eq. [3], including both of these boundary conditions.

### C. *Heat Transfer Across the Interfacial Gap*

Heat transfer across the interfacial gap governs the heat flux leaving the steel, $q_{int}$, to enter the mold. To calculate this at every position down the mold, the model evaluates an effective heat-transfer coefficient ($h_{gap}$) between the surface temperature of the steel shell ($T_s$) and the hot face of the mold wall ($T_{mold}$):

$$q_{int} = h_{gap} ( T_s - T_{mold} ) \qquad [4]$$

$$h_{gap} = 1 \Big/ \left( \left( r_{contact} + \frac{d_{air}}{k_{air}} + \frac{d_{solid}}{k_{solid}} \right) + 1 \Big/ \left( 1 \Big/ \left( \frac{d_{liquid}}{k_{liquid}} + \frac{d_{eff}}{k_{eff}} \right) + h_{rad} \right) \right) \qquad [5]$$

Heat conduction depends on the thermal resistances of four different layers of materials contained in the gap: the oscillation marks, liquid slag, solid slag, and a possible air gap. These depend on the time-averaged thickness profiles down the mold of the different layers and their corresponding thermal conductivities. The model for gap heat conduction is illustrated in Figures 3 and 6. The most important resistances are usually the slag layers, whose thicknesses are calculated as described in the next section. The latent heat evolved by liquid-slag solidification is less than 3 pct of the heat transferred across the gap, so it is neglected in this model.

The equivalent air gap ($d_{air}$) is specified as input data and includes contact resistances[46] at the slag/shell and slag/mold interfaces. It may also include a gap due to shrinkage of the steel shell, which can be calculated using a separate thermal-stress model.[12] The shrinkage gap is affected by the mold taper and also by mold distortion, which can be calculated by another model.[10] This gap is important when simulating down positions near the corner.

All nonuniformities in the flatness of the shell surface are incorporated into the model through the prescribed oscillation-mark depth ($d_{mark}$) and width ($L_{mark}$), as pictured in Figure 4. Assuming shallow triangle-shaped marks or depressions, $d_{osc}$ is the volume-averaged oscillation-mark depth:

$$d_{osc} = \frac{0.5\, L_{mark}\, d_{mark}}{L_{pitch}} \quad [6]$$

where $L_{pitch}$ is the ratio of the casting speed to the oscillation frequency.

The oscillation marks affect heat transfer in two different ways. First, the oscillation marks consume mold slag, so they affect the slag-layer thicknesses, as described in Section III–F. Second, they reduce heat conduction by effectively providing an extra gap. This extra gap is represented by $d_{eff}$, calculated based on a heat balance[47] which produces the same total heat flux as found by combining the heat fluxes across the two parallel conduction paths (at or adjacent to the oscillation mark), averaged spatially ($z$ direction) using an appropriate weighted average.

$$d_{eff} = \frac{0.5\, L_{mark}\, d_{mark}}{(L_{pitch} - L_{mark})\left(1 + 0.5\dfrac{d_{mark}}{d_{liquid} + d_{solid}}\dfrac{k_{gap}}{k_{mark}}\right) + L_{mark}} \quad [7]$$

$$k_{gap} = \left(d_{liquid} + d_{solid}\right) \Big/ \left(\frac{d_{solid}}{k_{solid}} + 1 \Big/ \left(\frac{k_{liquid}}{d_{liquid}} + h_{rad\_liquid}\right)\right) \quad [8]$$

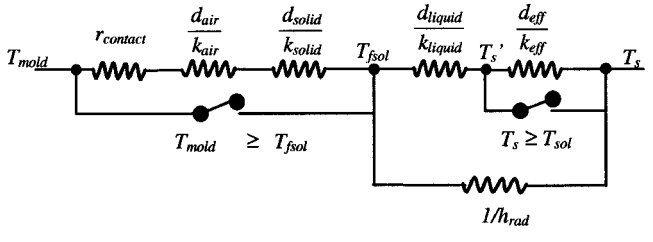


Fig. 3—Thermal resistances used in the interface model.

The oscillation marks are assumed to be filled with either slag, air, or a mixture, depending on the local shell-surface temperature. This governs the value of $k_{mark}$.

Except for perhaps a microscopically thin glassy surface layer, experience has shown that the cold slag layer adjacent to the mold wall is usually crystalline[48,49] and, thus, opaque. Thus, radiation occurs only across the semitransparent hot glassy or liquid layer above $T_{fsol}$,[50,51] according to Eq. [9], as shown in Figure 3:

$$h_{rad} = \frac{m^2\sigma\left(T_{sK}^2 + T_{fsolK}^2\right)\left(T_{sK} + T_{fsolK}\right)}{0.75a\left(d_{liquid} + d_{eff}\right) + \dfrac{1}{\varepsilon_{slag}} + \dfrac{1}{\varepsilon_{steel}} - 1} \quad (T_{mold} < T_{fsol}) \quad [9]$$

where $m$ is the slag refractive index; $T_{sK}$ and $T_{fsolK}$ are $T_s$ and $T_{fsol}$ expressed in Kelvin, respectively; $a$ is the average absorption coefficient of the slag, assuming graybody radiation ($\varepsilon_{slag} = 0.9$). If the liquid slag runs out, so that $T_s < T_{fsol}$, then $h_{rad} = 0$. In the unlikely event that $T_{mold} \geq T_{fsol}$, $\varepsilon_{slag}$ would be replaced by $\varepsilon_{mold}$, and $T_{fsol}$ by $T_{mold}$ in Eq. [9]. Jenkins showed that this simple equation to characterize radiation with absorption across a gap (Eq. [9]) is accurate to within 10 pct relative to a full multiview factor analysis including radiation-conduction.[52] This is sufficiently accurate, because the radiation component itself usually contributes only on the order of 10 pct of the gap heat transfer.

### D. *Mass and Momentum Balance on Powder Slag Layers*

Slag is assumed to flow down the gap as two distinct layers: solid and liquid. The solid layer is assumed to move at a time-averaged velocity ($V_{solid}$) which is always between zero and the casting speed, according to the input solid-slag speed ratio ($f_v$).

$$V_{solid} = f_v \cdot V_c \quad [10]$$

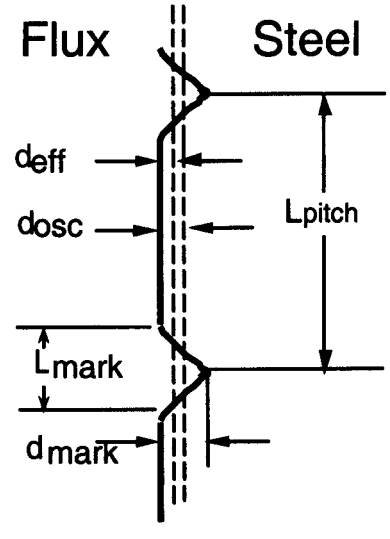


Fig. 4—Model treatment of oscillation marks.

The downward-velocity profile across the liquid slag layer is governed by the simplified Navier–Stokes equation, assuming laminar Couette flow:

$$\frac{\partial}{\partial x}\left(\mu\frac{\partial V_z}{\partial x}\right) = (\rho_{steel} - \rho_{slag})\, g \qquad [11]$$

A small body force opposing flow down the wide face gap is created by the difference between the ferrostatic pressure from the liquid steel ($\rho_{steel}\, g$), transmitted through the solid steel shell, and the average weight of the slag ($\rho_{slag}\, g$) The time-averaged velocity of the liquid slag ($V_z$), described by Eq. [11], is subjected to boundary conditions constraining it to the casting speed on its hot side and to the solid-slag velocity ($V_{solid}$) on its cold side.

The viscosity of the molten slag ($\mu(T)$) is assumed to vary exponentially with temperature:

$$\mu = \mu_o \left(\frac{T_o - T_{fsol}}{T - T_{fsol}}\right)^n \qquad [12]$$

where the parameters $T_{fsol}$ and $n$ are chosen empirically to fit measured data and $\mu_o$ is the viscosity measured at the reference temperature, $T_o$, usually chosen to be 1300 °C. A typical curve obtained with this function is shown in Figure 5 together with the measured viscosities by Lanyi that it was fit to match.[53] Mold slags in service absorb some $Al_2O_3$ from the steel, which changes their properties, including decreasing the solidification temperature.[53,54] The second curve in Figure 5 was constructed for a reported solidification temperature of 1045 °C and viscosity at 1300 °C of 1.1 Poise and was used later in model calibration.

By approximating the temperature across the gap to vary linearly, Eqs. [10] through [12] can be solved for the time-averaged velocity distribution across the slag layers, which is illustrated in Figure 6. Integrating across the liquid region yields an average velocity for the liquid layer ($\overline{V}_{liquid}$) of

$$\overline{V}_{liquid} = \frac{(\rho_{slag} - \rho_{steel})\, g d_{liquid}^2}{\mu_s\, (n+2)^2\, (n+3)} + \frac{V_c + V_{solid}\, (n+1)}{(n+2)} \qquad [13]$$

where $\mu_s$ is the slag viscosity at the liquid layer/steel shell interface. A mass balance was imposed to match the measured (known) powder consumption ($Q_{slag}$ (kg/m$^2$)) with the total molten slag flow rate past every location down the interfacial gap, neglecting the carbon-content component, which burns off. This consumption rate is expressed as mass of slag per unit area of the strand surface, which can be found from the consumption per mass of product ($M_{slag}$ (kg/ton)):

$$Q_{slag}\,(\text{kg/m}^2) = M_{slag}\,(\text{kg/ton}) \times \rho_{steel} \times \frac{W \times N}{2\,(W+N)} \qquad [14]$$

where $W$ is the slab width and $N$ is the slab thickness. Slag can be carried downward by the solid layer, the liquid layer, and in the oscillations marks:

$$\frac{Q_{slag} \times V_c}{\rho_{slag}} = V_{solid}\, d_{solid} + \overline{V}_{liquid}\, d_{liquid} + V_c\, d_{osc} \qquad [15]$$

The liquid- and solid-layer thicknesses are obtained by solving a fourth-order polynomial equation, found by combining Eqs. [5] and [15]. The transport of slag by the oscillation marks depends on the lubrication state, discussed next.

Three different regions are distinguished down the mold, according to the lubrication condition. Close to the meniscus, a solid slag rim exists against the mold wall. Its thickness profile must be specified, as it depends on transient phenomena not yet in the model.

The second region, shown in Figure 6, allows the solid slag layer to move at the slow time-averaged velocity $V_{solid}$. It always also includes oscillation marks filled with molten slag and a continuous liquid slag layer, which remains

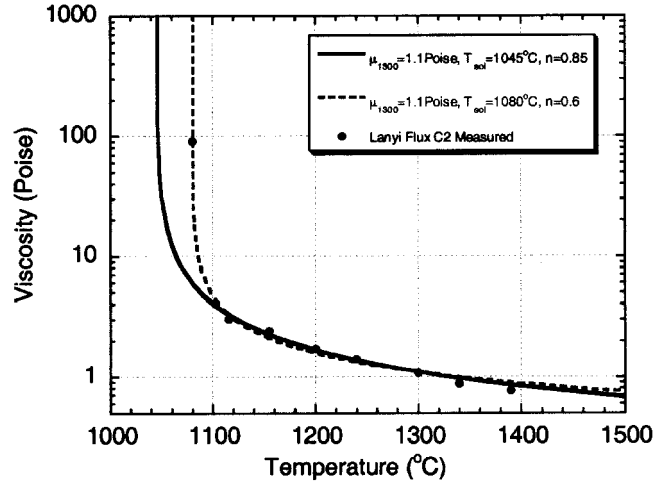


Fig. 5—Comparison of model mold slag viscosity curves and measurements.[53]

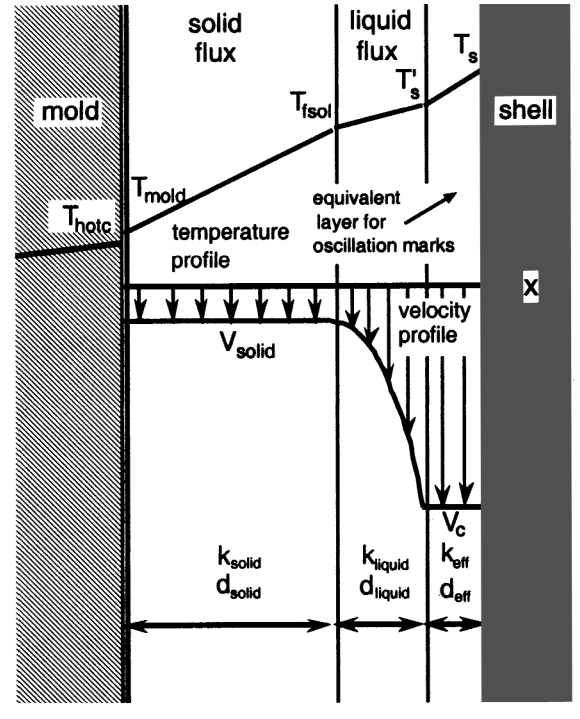


Fig. 6—Velocity and temperature profiles assumed across interfacial gap.

present so long as the outer-surface temperature of the steel ($T_s'$) exceeds the slag solidification temperature, $T_{fsol}$:

$$T_s' = T_s - q_{int} \times \frac{d_{eff}}{k_{mark}} \quad [16]$$

Slag in the oscillation marks remains liquid longer, due to the higher local shell temperature at their roots ($T_s$). Once the oscillation-mark roots cool below the slag solidification temperature, however, the slag entrapped in them solidifies. This defines the third region, which consists of totally solid slag, moving downward at the uniform speed. The oscillation marks no longer transport slag and, so, become filled with air. The transition between the second and third regions is gradual.

It is important to emphasize that this model represents steady, time-averaged behavior only. To investigate transient phenomena, a transient version of this model is being developed to calculate stress inside the slag layer based on a force balance with friction, which is described elsewhere.[55]

### E. *Heat Conduction in the Mold*

A 2-D, steady-state temperature within a rectangular vertical section through the upper portion of the mold is calculated assuming constant conductivity:

$$\frac{\partial^2 T}{\partial x^2} + \frac{\partial^2 T}{\partial z^2} = 0 \quad [17]$$

This equation is solved using a standard Fourier-series product solution,[56] applying a fixed heat flux of $q_{int} = -k_{mold}\,\partial T/\partial x$, and convection, $h_{water}$, and $T_{water}$ as boundary conditions, as shown in Figure 7(a). This copper domain is generally chosen to extend from the top of the mold to 100 mm below the meniscus. Below this meniscus region, heat flow is 1-D through the thickness. The temperature at the copper hot face ($T_{hotc}$) is then

$$T_{hotc} = T_{water} + q_{int}\left(\frac{1}{h_{water}} + \frac{d_{mold}}{k_{mold}}\right) \quad [18]$$

where $d_{mold}$ is the copper mold thickness calculated in Appendix B. Coating layers are incorporated as needed to find the mold hot-face temperature ($T_{mold}$) by adding extra $d_{coat}/k_{coat}$ resistances to Eq. [18] as needed. In addition to the heat flux across the interface ($q_{int}$), this calculation requires the initial cooling-water temperature ($T_{water}$) input as a boundary condition, and the effective water heat-transfer coefficient ($h_{water}$), discussed as follows.

### F. *Convection to the Cooling Water*

The effective heat-transfer coefficient between the cooling water and the cold face ("water side") of the mold is calculated to include a possible resistance due to scale deposits on the surface of the cooling-water channels:

$$h_{water} = 1\Big/\left(\frac{d_{scale}}{k_{scale}} + \frac{1}{h_{fin}}\right) \quad [19]$$

To account for the complex nature of heat flow in the undiscretized width direction of the mold, the heat-transfer coefficient between the mold cold face and the cooling water ($h_{fin}$) incorporates heat flow to both the root and sides of the water channels, the latter treated as heat-transfer fins.

$$h_{fin} = \frac{h_w\, w_{ch}}{L_{ch}} + \frac{\sqrt{2h_w\, k_{mold}\,(L_{ch} - w_{ch})}}{L_{ch}} \tanh\sqrt{\frac{2h_w\, d_{ch}^2}{k_{mold}\,(L_{ch} - w_{ch})}} \quad [20]$$

where the mold-geometry parameters $L_{ch}$, $w_{ch}$, and $d_{ch}$ are shown in Figure 7(b). The heat-transfer coefficient between the water and the sides of the water channel ($h_w$) is calculated assuming turbulent flow through an equivalent-diameter pipe using the empirical correlation of Sleicher and Reusse,[57] which is reported[58] to be more accurate than other relations such as that of Dittus and Boelter:[59]

$$h_w = \frac{k_{water}}{D}\left(5 + 0.015\,\mathrm{Re}_{waterf}^{c_1}\,\mathrm{Pr}_{waterw}^{c_2}\right) \quad [21]$$

where $D = 2w_{ch}\,d_{ch}/(w_{ch} + d_{ch})$ is the equivalent diameter of the water channel, and $c_1 = 0.88 - 0.24/(4 + \mathrm{Pr}_{waterw})$ and $c_2 = 0.333 + 0.5e^{-0.6\,\mathrm{Pr}_{waterw}}$ are empirical constants.

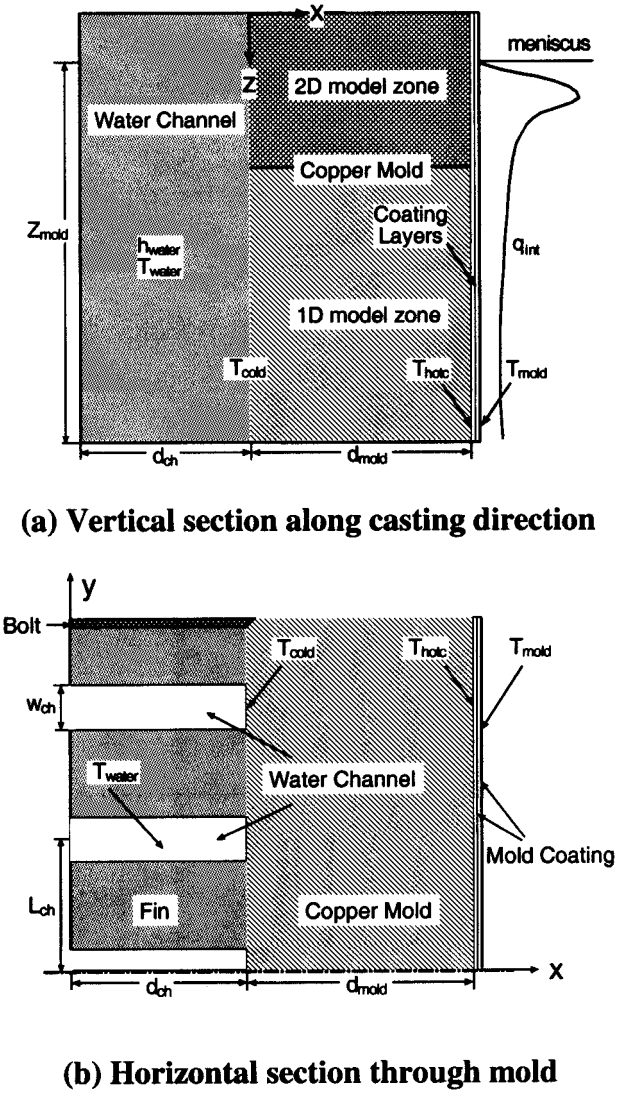


Fig. 7—Simulation domain in mold (*a*) vertical section along casting direction and (*b*) horizontal section through mold.

The presence of the water slots can either enhance or diminish the heat transfer, relative to a tube mold with uniform thickness ($d_{mold}$) such as used in billet casting. Deep, closely spaced slots augment the heat-transfer coefficient ($h_{fin}$ is larger than $h_w$), while shallow, widely spaced slots inhibit heat transfer. In most molds, $h_{fin}$ and $h_w$ are very close.

Although it slightly underpredicts the mold temperature, Eq. [20] was shown, through comparison with many 3-D computations for a variety of typical slab-casting mold geometries and conditions, to match the temperature within 1 pct at the water-slot root and from 0.1 to 6 pct at the hot face.[47,60] For a typical hot-face temperature of 190 °C and water temperature of 30 °C, it gives maximum errors of 2 °C and 10 °C. It is most accurate for molds with either deep, closely spaced slots[47] or very wide slots,[60] where the cold-face temperature is most nearly constant, as assumed in Eq. [20].

## G. *Spray zones below the mold*

Below the mold, heat flux from the strand surface varies greatly between each pair of support rolls, according to the spray-nozzle cooling, based on water flux ($h_{spray}$); radiation ($h_{rad\_spray}$); natural convection ($h_{conv}$); and heat conduction to the rolls ($h_{roll}$), as shown in Figure 8. Incorporating these phenomena enables the model to simulate heat transfer during the entire continuous casting process. The heat extraction due to water sprays is a function of water flow[61] of the following form:

$$h_{spray} = A \times Q_{water}^{c} \times (1 - b \times T_{spray}) \qquad [22]$$

where $Q_{water}$ (L/m$^2$ s) is water flux in the spray zones, and $T_{spray}$ is the temperature of the cooling-water spray. In Nozaki's empirical correlation,[62] $A = 0.3925, c = 0.55$, and $b = 0.0075$, which has been used successfully by other modelers.[61,63]

Radiation is calculated by

$$h_{rad\_spray} = \sigma \times \varepsilon_{steel} (T_{sK} + T_{amb\,K}) (T_{sK}^2 + T_{amb\,K}{}^2) \qquad [23]$$

where $T_{amb}$ is the ambient temperature and $T_{sK}$ and $T_{ambK}$ are $T_s$ and $T_{amb}$ expressed in Kelvin. Natural convection is treated as a constant input for every spray zone. For water cooling only, it is not very important, so it was simplified to 8.7 W/m$^2$K everywhere. Larger values can be input for $h_{conv}$ to reflect the stronger convection when there is air mist in the cooling zone. Heat extraction into the rolls is calculated based on the fraction of heat extraction to the rolls ($f_{roll}$), which is calibrated for each spray zone:

$$h_{roll} = \frac{f_{roll}}{L_{roll\ contact}\,(1 - f_{roll})} [(h_{rad\_spray} + h_{conv} + h_{spray}) L_{spray} + (h_{rad\_spray} + h_{conv})(L_{spray\ pitch} - L_{spray} - L_{roll\ contact})] \qquad [24]$$

A typical $f_{roll}$ value of 0.05 produces local temperature drops beneath the rolls of about 100 °C. Beyond the spray zones, heat transfer simplifies to radiation and natural convection.

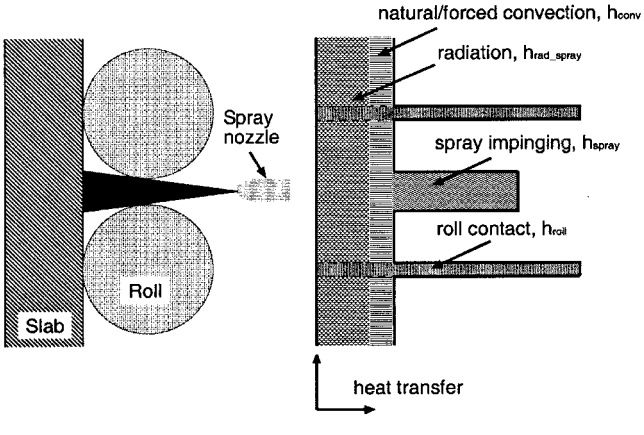


Fig. 8—Schematic of spray zone region.

## H. *Solution Methodology*

The model requires simultaneous solution of three different systems of equations: 1-D transient heat conduction and solidification of the steel shell, 2-D steady-state heat conduction in the mold, and the equations balancing heat, mass, and momentum in the gap. The simulation starts by setting the initial steel and mold temperatures to the pouring temperature and inlet cooling-water temperature, respectively. Phase-transformation temperatures and phase-fraction temperature curves are then calculated, using one of the methods described in the next section. Then, each time step begins by rearranging and solving Eqs. [5] and 15 simultaneously for $d_{liquid}$ and $d_{solid}$, based on heat and mass balance at the previous time step. The heat flux $q_{int}$ is then calculated according to Eqs. [4] and [5], which is the boundary condition for both steel and mold domains. The heat-transfer coefficient $h_{water}$ is calculated according to cooling-channel conditions with Eqs. [19] through [21] and is used to obtain mold temperatures. Applying the superheat flux-boundary condition (Eq. [2]) as an internal heat source at the steel solid/liquid interface, the model uses an explicit, central finite-difference algorithm originally developed by Pehlke[64] to solve Eq. [3] for the shell temperature at each time step (Appendix A). This limits the maximum time-step size ($\Delta t$). When a node temperature drops below the liquidus temperature, its solid fraction is calculated from the latent heat evolved, and then the node temperature is adjusted[65] (Eq. [A6]) according to the phase fraction–temperature curves, described in Section IV–A. The results are used as initial conditions for the 2-D mold calculation, which solves Eq. [17] analytically, relating the distance down the mold ($z$) to the time in the shell through the casting speed. Subsequently, the entire 1-D shell-solidification model in the 2-D mold region is recomputed using the new 2-D mold temperatures as its boundary condition. This stepwise coupling procedure alternates between models until the 1-D mold temperatures converge to match the 2-D results within 3 °C. This produces a self-consistent prediction, which is stable for all coupled simulations investigated and usually converges in three to four iterations. Figure 9 gives a flow chart of the whole procedure.

The model has been incorporated into a user-friendly FORTRAN program, CONID.[66] A 100-second-long simulation with a 0.004-second time step and 100-node mesh runs on a PENTIUM* III personal computer (using 3.1 Mbytes of memory) in about 30 seconds.

*PENTIUM is a trademark of the Intel Corporation, Santa Clara, CA.

## IV. STEEL PROPERTIES

The program includes several different choices for steel properties, including simple constants input by the user. By default, the liquidus temperature, solidus temperature, phase-fraction curve, thermal conductivity, specific heat, and thermal linear expansion are all calculated as functions of composition and temperature. The steel density ($\rho_{steel}$), latent heat ($L_f$), and steel-surface emissivity ($\varepsilon_{steel}$) are constants. For carbon steel, $\rho_{steel} = 7400$ kg/m$^3$, $L_f = 271$ kJ/kg, and $\varepsilon_{steel} = 0.8$.

### A. *Phase Fraction*

By default, equilibrium lever-rule calculations are performed on an Fe-C phase diagram, whose phase-field lines are specified as simple linear functions of alloy content (including the influences of Si, Cr, Mn, Ni, Mo, Cu, Ti, P, S, Al, V, N, Nb, and W) reported by Kagawa and Okamoto[67] in order to calculate the steel liquidus, solidus, and peritectic temperature and phase fractions. Alternatively, the user can choose a nonequilibrium microsegregation model to find these values, based on an analytical Clyne–Kurz-style equation developed by Won and Thomas,[68] which was extended in this work to include the effects of 14 elements, given in Appendix C. For a 0.044 pct C, 0.022 pct Mn, 0.006 pct S, 0.01 pct P, 0.009 pct Si, and 0.049 pct Al plain-carbon steel, the equilibrium-phase-diagram model calculates $T_{liq} = 1528$ °C and $T_{sol} = 1509$ °C, while with a 10 °C/s cooling rate, the segregation model gives $T_{liq} = 1532$ °C and $T_{sol} = 1510$ °C. Figure 10 shows the solid-fraction temperature curve in the mushy zone, obtained from both models. Both models produce similar results. The surprising finding that the equilibrium model produces slightly lower transformation temperatures shows that differences in the coefficients which define the alloy-dependent equilibrium lines are more important than the nonequilibrium effects due to segregation at the typical cooling rates, dendrite-arm spacing, and compositions considered.

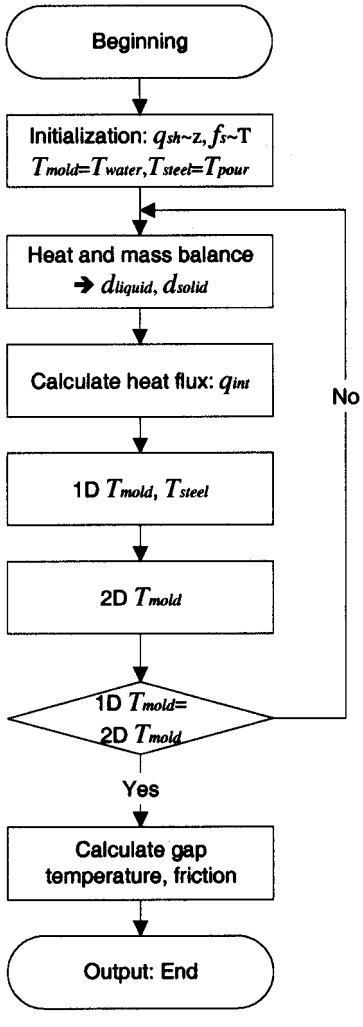


Fig. 9—Flow chart of CON1D program with 1-D steel solidification model and 2-D mold heat conduction model.

### B. *Thermal Conductivity of Steel*

The thermal conductivity of carbon steel is calculated as a function of temperature, carbon content, and phase fraction, which was fitted from measured data compiled by K. Harste.[44] The specific functions are listed in Appendix D. The stainless steel thermal conductivity is calculated according to a fitted equation based on measured data compiled by Pehlke.[45] Figure 11 compares some typical

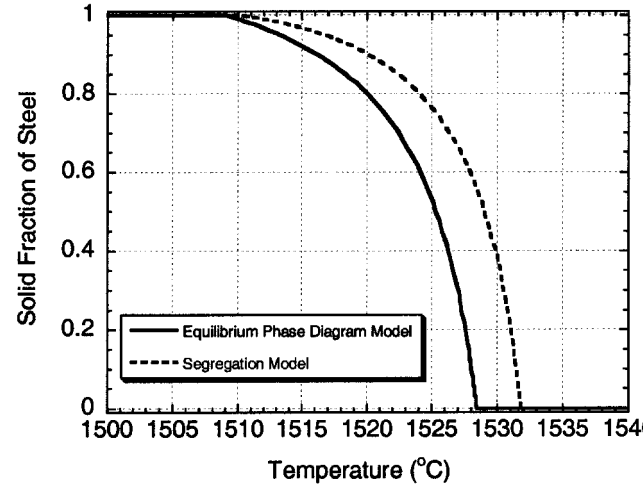


Fig. 10—Phase fraction variation with temperature in mushy zone.

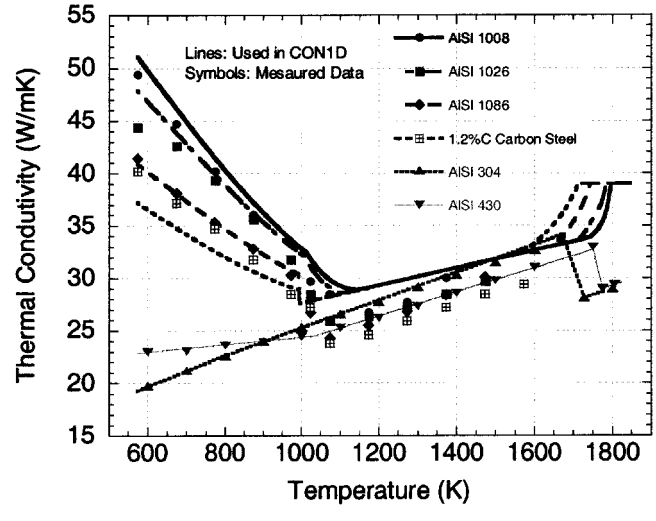


Fig. 11—Comparison of model thermal conductivities and measurements.[45]

plain-carbon steel, austenitic stainless steel, and ferritic stainless steel conductivities. The thermal conductivity of the liquid is not artificially increased, as is common in other models, because the effect of liquid convection is accounted for in the superheat-flux function, which is calculated by models which fully incorporate the effects of turbulent flow.

### C. *Effective Specific Heat of Steel*

The specific heat is calculated as a function of temperature, carbon content, phase fraction and steel grade. Appendix D gives the specific-heat functions for carbon steel, found by differentiating the enthalpy curve from K. Harste.[44] Refer to Pehlke[45] for the specific-heat functions of stainless steel. When the steel temperature is between the solidus and liquidus temperatures, the latent heat is evolved using the liquid-phase-fraction curve found previously. The effective specific heat is then defined as

$$C_p^* = \frac{dH}{dT} = C_p - L_f \frac{df_s}{dT} \quad [25]$$

Figure 12 shows the specific-heat curve of AISI 1026 carbon steel using the microsegregation model, compared with measured data.[45] The curves for other alloys, such as those used later, are similar except for within the mushy region. So long as it properly matches the total latent heat, its exact shape has little effect on the shell growth or surface temperature.

### D. *Thermal Linear Expansion of Steel*

By default, the thermal linear expansion (TLE) needed for shrinkage and ideal taper calculations is computed as a function of steel density:

$$\text{TLE} = \sqrt[3]{\frac{\rho_0}{\rho(T)}} - 1 \quad [26]$$

where $\rho_0 = \rho_{steel}$. The composition and temperature-dependent steel-density function for carbon steel ($\rho(T)$) is taken from measurements tabulated by Harste[44] and is listed in Appendix D. A constant density ($\rho_{steel}$) is adopted for the heat-flow calculations in order to enforce constant mass in the fixed-domain computation.

Alternatively, the user may input a thermal linear-expansion coefficient ($\alpha$), so that

$$\text{TLE} = \alpha(T - T_{sol}) \quad [27]$$

This is done for stainless steel, where the value of $\alpha$ is taken from Pehlke.[45]

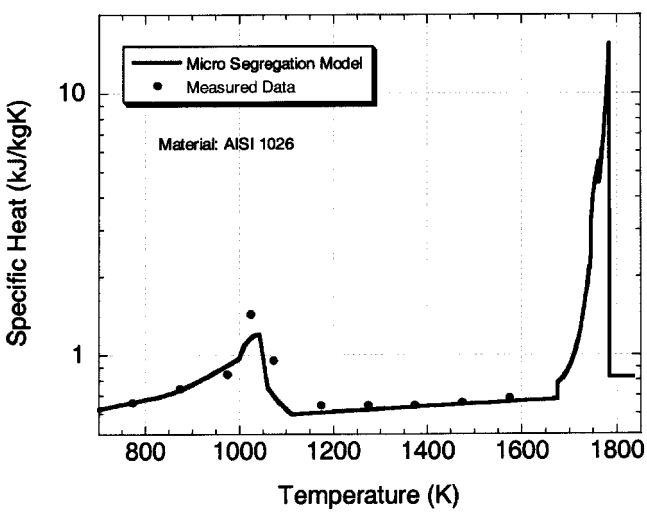


Fig. 12—Comparison of model specific heat curve and measurements.[45]

## V. MODEL VALIDATION

The internal consistency and accuracy of the various components of this model have been verified through extensive comparison with analytical solutions. The accuracy of the 2-D mold heat-transfer model at the meniscus region was evaluated by comparison with full 3-D finite-element model computations on separate occasions using ABAQUS[69] and with an in-house code.[70] In both cases, the CON1D model predictions matched within the uncertainties associated with mesh refinement of the 3-D model. The fin heat-transfer equation was compared with 3-D model computations by Thomas *et al.*[71] and Langeneckert,[60] as already discussed. Its accuracy is acceptable except near thermocouples located in a region of complex heat flow. Its accuracy there can be improved by incorporating an "offset" distance, as discussed elsewhere.[26,60] Other obvious checks include ensuring that the temperature predictions match at the transition between at 2-D and 1-D regions, which also indicates when heat flow is 1-D.

The solidification model is verified here through comparison with an analytical solution for 1-D heat conduction with phase change.[72] This solution assumes a constant shell-surface temperature and constant steel properties. Table I lists the constants used in both the analytical solution and the CON1D validation case, which are chosen for typical conditions expected in practice. The difference between the steel liquidus and solidus temperatures is only 0.1 °C to approximate the single melting temperature assumed in analytical solution, which is set to the mean of $T_{liq}$ and $T_{sol}$ used in CON1D. The pour temperature is set to the liquidus because the superheat is neglected in the analytical solution. For the CON1D model, the time-step size $\Delta t$ is 0.004 seconds and the node spacing is 0.5 mm.

Figure 13 compares results from the analytical solution and CON1D model for (a) the temperature distribution through the shell at different times and (b) the growth of the shell thickness with time. The results show that the predictions of the CON1D model are very accurate, so the same time step and mesh size are used in the following cases.

**Table I. Constants Used in Analytical Solution and Validation Case**

| | | |
|---|---|---|
| Conductivity, $k_{steel}$ | 30 | W/mK |
| Specific Heat, $Cp_{steel}$ | 670 | J/kgK |
| Latent Heat, $L_f$ | 271 | kJ/kg |
| Density, $\rho_{steel}$ | 7400 | kg/m$_3$ |
| Melting Temperature, $T_{melt}$ | 1509.05 | °C |
| Liquidus Temperature, $T_{liq}$ | 1509.1 | °C |
| Solidus Temperature, $T_{sol}$ | 1509 | °C |
| Shell Surface Temperature, $T_s$ | 1000 | °C |

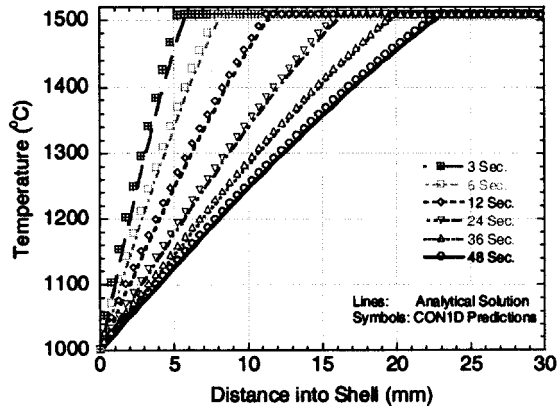


(a) Shell temperature distribution

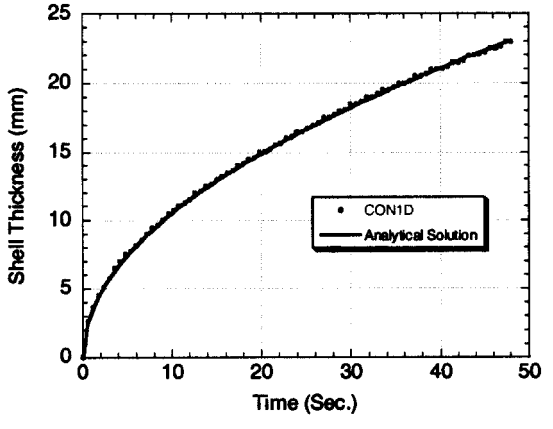


(b) Shell growth

Fig. 13—Comparison of model results and analytical solution: (*a*) shell temperature distribution and (*b*) shell growth.

## VI. MODEL CALIBRATION

Having shown the model to be internally consistent, it cannot be used quantitatively until it is calibrated to match measurements on the specific operating caster of interest. This step is necessary because so many of the inputs to the model are uncertain.

To date, the model has been calibrated to match many different casters, including slabs at BHP LPD (Whyalla, South Australia), LTV Steel (Cleveland, OH),[73] AK Steel (Mansfield, OH),[26] Allegheny Ludlum (Brackenridge, PA),[74] Columbus Stainless Steel (Middleburg, South Africa),[70] Siderar (Buenos Aires, Argentina),[85] and China Steel (Taiwan, Republic of China); thin slabs at Nucor (Crawfordsville, IN)[75] and POSCO (Seoul, South Korea);[76] blooms at BHP RBPD (Newcastle, New South Wales);[77] and billets at POSCO (Pohang, South Korea).[78] In order to calibrate the model, it is simply run several times, using trial and error, to find values of the model parameters that allow the model predictions to match all of the known measurements. Those measurements can include the cooling-water temperature rise, the time-averaged temperature of any thermocouples embedded in the mold, the thickness profile of breakout shells, the thickness of solidified-mold powder layers and slag rims, and the temperature histories of any thermocouples embedded in the strand.

Specifically, adjustments can be made to the velocity of the solid slag layer, the value of the contact resistances down the mold, and even the thermal properties of the mold slag. Other influential input parameters include the average powder consumption rate and the average oscillation-mark depth and width.

In a slab caster with properly designed taper, there should not be any air gap due to shrinkage down the center of the wide face. This is because ferrostatic pressure pushes the long, wide, weak shell against the mold to maintain as close a contact as possible. This greatly simplifies model calibration when simulating a slice through the wide face of the mold and shell.

The following sections report on the calibration, validation, and results of simulations performed for two sets of conditions given in Tables II and V. Input parameters for the standard case, Table II, were calibrated to match the casting conditions of the 0.225 × 1.78 m slabs of low-carbon steel cast at LTV Steel (Cleveland, OH), where mold thermocouple temperatures, cooling-water temperature-rise, and breakout-shell measurements were available.[71,79] The steel composition is 0.044 pct C, 0.022 pct Mn, 0.006 pct S, 0.01 pct P, 0.009 pct Si, and 0.049 pct Al.

### A. *Mold Cooling-Water Temperature Rise*

The first step in model calibration is to match the total heat extracted in the mold with the measured temperature increase of the mold cooling water. The average rate of heat extracted from the mold per unit surface area ($Q$) is found from

$$Q = \frac{V_c}{Z_{\text{mold}}} \sum_{\text{mold}} q_{\text{int}} \Delta t \qquad [28]$$

This heat-transfer rate should equal the temperature increase of the mold cooling water ($\Delta T_{\text{water}}$) flowing through the "hot" channels, located adjacent to the slab width area:

$$\Delta T_{\text{water\_hot channels}} = \sum_{\text{mold}} \frac{q_{\text{int}} L_{ch} V_c \Delta t}{\rho_{\text{water}} C_{\text{pwater}} V_{\text{water}} w_{ch} d_{ch}} \qquad [29]$$

This equation assumes that the cooling-water slots have locally uniform rectangular dimensions, $w_{ch}$ and $d_{ch}$, and spacing, $L_{ch}$. Heat entering the hot face (between two water channels) is assumed to pass straight through the mold to heat the water flowing through the cooling channels.

To compare with the measured water-temperature increase, the a forementioned prediction is modified as follows to account for missing slots due to bolts or water slots, or slots that are beyond the slab width and, so, do not participate in heat extraction:

$$\Delta T_{\text{water\_total channel}} = \Delta T_{\text{water\_hot channels}} \frac{w_{ch} \times d_{ch} \times W/L_{ch}}{\text{total channel area}} \qquad [30]$$

Using reported slag properties and consumption rate (Table II), the heat flux was calibrated to match the measured temperature rise of 7.1 °C by adjusting the solid-slag speed ratio, $f_v$, to 0.175. The corresponding temperature rise in just the hot channels is predicted to be 7.5 °C.

### B. *Mold Temperatures*

The next step in calibration of CON1D is to further adjust the model parameters to match the measurements

of thermocouples embedded in the walls of the operating casting mold. This step is very constrained, however, as every change that causes a local increase in heat flux must be balanced by a corresponding decrease elsewhere, in order to maintain the balance with the cooling water already achieved.

In this example (Table II), the slag-rim shape in region I was chosen to decrease linearly from 0.8 mm at the meniscus to 0.5 mm at 15 mm below the metal level, which is near to the position of peak heat flux. The peak heat-flux position should not be confused with the location of the peak mold temperature, which is usually about 35 mm below the heat-flux peak (55 mm below the meniscus, in this case). Assuming no air gap in the interface for this wide-face simulation, the contact resistances and scale thicknesses are other adjustable input conditions to match the mold thermocouple measurements. Here, a 0.02 mm scale layer was assumed for the top 305 mm, where specially designed inserts had been installed to increase the local cooling-water velocity,[79] and a 0.01 mm scale layer was assumed for the bottom remainder of the mold. These thicknesses are in accordance with plant observations that the hot region had a thicker scale layer.[80]

**Table II. Standard Input Conditions (Case 1)**

| | | |
|---|---|---|
| Carbon content, C pct | 0.044 | pct |
| Liquidus temperature, $T_{liq}$ | 1529 | °C |
| Solidus temperature, $T_{sol}$ | 1509 | °C |
| Steel density, $\rho_{steel}$ | 7400 | kg/m$^2$ |
| Steel emissivity, $\varepsilon_{steel}$ | 0.8 | — |
| Fraction solid for shell thickness location, $f_s$ | 0.1 | — |
| Mold thickness at top (outer face, including water channel) | 56.8 | mm |
| Mold outer face radius, $R_o$ | 11.985 | m |
| Total mold length, $Z_{moldtotal}$ | 900 | mm |
| Total mold width | 1876 | mm |
| Scale thickness at mold cold face (inserts region/below), $d_{scale}$ | 0.02/0.01 | mm |
| Initial cooling water temperature, $T_{water}$ | 30 | °C |
| Water channel geometry, $d_{ch} \times w_{ch} \times L_{ch}$ | $25 \times 5 \times 29$ | mm$^3$ |
| Cooling water velocity, $V_{water}$ | 7.8 | m/s |
| Mold conductivity, $k_{mold}$ | 315 | W/mK |
| Mold emissivity, $\varepsilon_{mold}$ | 0.5 | — |
| Mold powder solidification temperature, $T_{fsol}$ | 1045 | °C |
| Mold powder conductivity, $k_{solid}/k_{liquid}$ | 1.5/1.5 | W/mK |
| Air conductivity, $k_{air}$ | 0.06 | W/mK |
| Slag layer/mold resistance, $r_{contact}$ | $5.0 \times 10^{-9}$ | m$^2$K/W |
| Mold powder viscosity at 1300 °C, $\mu_{1300}$ | 1.1 | Poise |
| Exponent for temperature dependence of viscosity, $n$ | 0.85 | — |
| Slag density, $\rho_{slag}$ | 2500 | kg/m$^3$ |
| Slag absorption factor, $a$ | 250 | m$^{-1}$ |
| Slag refractive index, $m$ | 1.5 | — |
| Slag emissivity, $\varepsilon_{slag}$ | 0.9 | — |
| Mold powder consumption rate, $Q_{slag}$ | 0.6 | kg/m$^2$ |
| Empirical solid slag layer speed factor, $f_v$ | 0.175 | — |
| Casting speed, $V_c$ | 1.07 | m/min |
| Pour temperature, $T_{pour}$ | 1550 | °C |
| Slab geometry, $W \times N$ | $1780 \times 225$ | mm × mm |
| Nozzle submergence depth, $d_{nozzle}$ | 265 | mm |
| Working mold length, $Z_{mold}$ | 810 | mm |
| Oscillation mark geometry, $d_{mark} \times w_{mark}$ | $0.45 \times 4.5$ | mm × mm |
| Mold oscillation frequency | 84 | cpm |
| Oscillation stroke | 10 | mm |
| Time-step, $dt$ | 0.004 | s |
| Mesh size, $dx$ | 0.5 | mm |

Figure 14 compares the predicted and measured temperatures at several locations down the LTV mold. The thermocouples were all 18.8 mm below the mold hot face. The agreement indicates the calibration of the model for these typical casting conditions. This figure also shows the predicted hot-face and cold-face temperature profiles. The sharp change in temperature is due to a sudden increase in water-channel depth, produced by experimental inserts used in the trial.[79] Note that the observed scale layer greatly increased the mold temperature, especially in the hot portion that contained the insert. Based on this insight, steps were taken to improve water quality to prevent this scale and improve mold life.[79]

### C. *Shell Thickness*

Having calibrated the model, the predicted shell-thickness profile is compared with measurements down a breakout shell that occurred under very similar castings conditions, as given in Figure 15. Shell thickness is defined in the model by interpolating the position between the liquidus and solidus isotherms with the temperature corresponding to the specified solid fraction ($f_s$), according to the phase-fraction–temperature relationship in Figure 10. In this sample case, $f_s = 0.1$, which is the only adjustable parameter remaining for model calibration. This is reasonable, as interdendritic liquid is held by surface tension during draining of the breakout.

To compare the predicted steady shell thickness with that of a breakout shell, a correction is needed to account for the solidification time that occurred while the liquid metal was draining during the breakout. Thus, the time in the steady

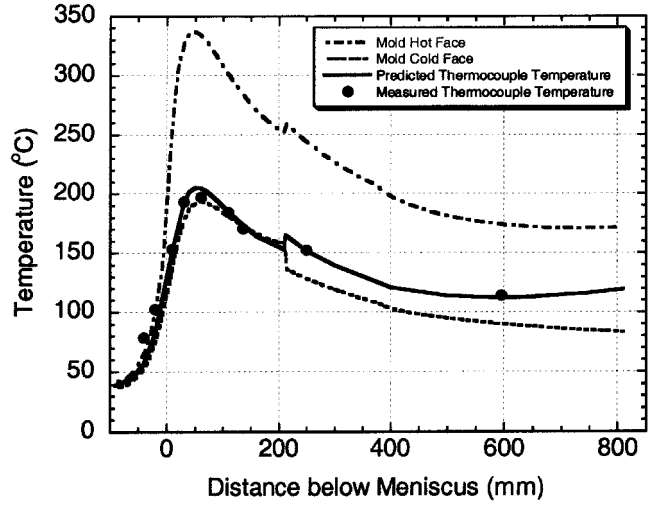


Fig. 14—Comparison of CON1D predicted and measured mold temperature.

simulation corresponds to distance down the breakout shell according to the relation

$$t = \frac{z}{V_c} + t_d \qquad [31]$$

where the "drainage time" ($t_d$) is the time for the metal level to drop from the meniscus to the breakout slice of interest ($z$). The drainage time is calculated based on the Bernoulli equation and a mass balance:[81]

$$t_d = \frac{\sqrt{Z_b} - \sqrt{Z_b - z}}{C_D \frac{\pi d_b^2}{4NW}\sqrt{\frac{g}{2}}} \qquad [32]$$

where the drainage coefficient is $C_D = 1$. For the present case, the position of the breakout hole from the meniscus is $Z_b = 1.524$ m; the slab thickness is $N = 0.225$ m; and the slab width is $W = 1.78$ m. Assuming that steel flow to the mold was shut off simultaneously as the metal level started to drop below the meniscus and that the breakout hole diameter ($d_b$) began at 50 mm and linearly grew to 90 mm by the time all liquid steel had drained, a transient shell profile can be calculated. Figure 15 gives the predicted shell thickness at both steady-state and transient conditions, compared with the breakout-shell measurements. The generally close match with the transient predictions tends to validate the model. The under-predicted shell thickness near the meniscus is likely due to a short interval of increased liquid flow into the mold after the breakout started and before level control and flow were shut off. This would have allowed the liquid level to move downward with the top of the breakout shell for a short time interval (not included in the model), thus providing additional solidification time at the very top of the breakout shell. This effect is commonly observed in breakout shells.

Growth of the shell naturally depends on both the interfacial and superheat fluxes. The superheat distribution is important to the narrow face, as Figure 2 shows that the two curves are of the same magnitude low in the mold, where the hot molten steel jet impinges against the solidifying shell. Figure 15 shows the shell thinning of the narrow face due to this jet-impingement effect.

Variation in the superheat flux is critical to shell growth down the narrow face and off-corner regions, where problems such as inadequate taper sometimes produce significant air gap(s). Together, the large superheat combined with decreased heat transfer across the interfacial gap can reduce shell growth. This was the subject of a significant study using the model, which was reported elsewhere.[82]

### D. *Powder-Layer Thickness*

The model predicts the thickness and velocity profiles expected in the powder layers in the interfacial gap. For example, Figure 16 shows the solid and liquid slag-layer thickness profiles expected for the standard conditions investigated here (Table II). It shows that the liquid slag layer runs out at 380 mm below the meniscus, where the liquid slag-layer/steel-shell interface temperature drops below the slag solidification temperature of 1045 °C, as shown in Figure 17. The total slag thickness continues to increase while there is still liquid coming from the oscillation marks. This is indicated in Figure 17, where the shell-surface temperature at the oscillation-mark roots still exceeds 1045 °C at mold exit. Although no reliable slag samples were obtained from this caster, these slag-thickness predictions of 0.5 to 1.5 mm are consistent with samples measured at similar plants.[47,76]

### E. *Shell-Surface Temperature*

Typical model predictions of the surface temperature in the mold are shown in Figure 17 for standard conditions. When the liquid slag layer runs out at 380 mm below the meniscus (Figure 16), the liquid entrapped in oscillation marks flows out and air fills in, which increases the resistance of the oscillation mark, so the temperature difference between the oscillation mark's root and peak increases also, as shown in Figure 17.

After existing the mold, the slab surface quickly reheats, and then it fluctuates greatly as it travels through the spray zones. Heat is extracted rapidly during contact with the support rolls and when passing the impingement zone of the cooling water from the spray nozzles, which each cause great temporary drops in surface temperature.

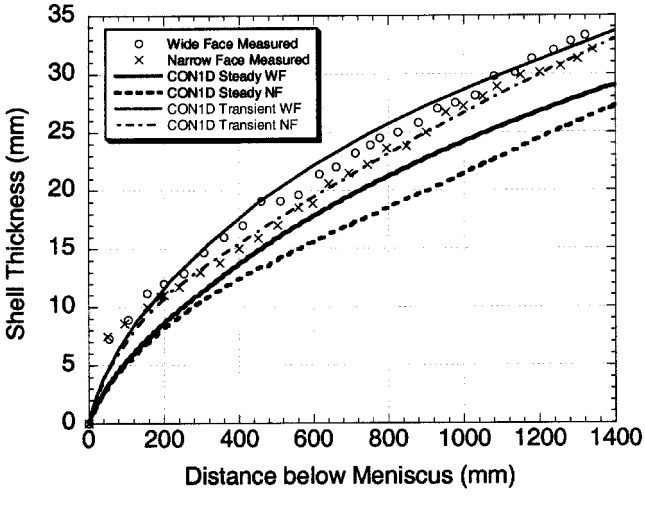


Fig. 15—Comparison of CON1D predicted and measured shell thickness.

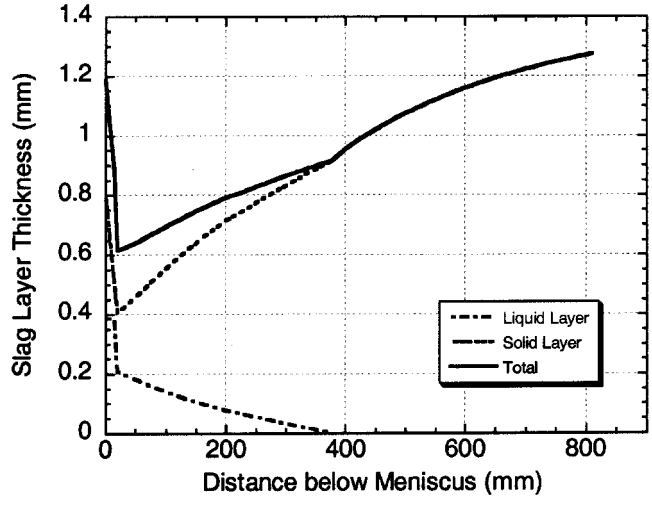


Fig. 16—Predicted slag layer thickness profiles.

Lacking accurate spray and roll contact heat-transfer coefficients, calibration of temperature predictions below the mold can be calibrated by adjusting the model parameters $f_{roll}$ and the spray coefficients (Table III) to match measurements such as roll cooling-water heat-extraction rate and thermocouple temperatures embedded in the strand. An example of such calibration is shown in Figure 18 for casting conditions measured at the China Steel #1 slab caster in Taiwan, Republic of China, given in Tables III and IV. The temperature measurements were achieved by feeding a block containing several thermocouples into the mold just before "tail-out" at the end of casting. The thermocouple tips extending through the bottom of the block were soon frozen into the strand. The last several meters of steel before the end of the cast ensured that the recorded temperature histories would be typical, while allowing the insulated tube of thermocouple wires extending from the top of the block to follow the strand through the caster with minimal damage. The distance of each thermocouple from the surface was measured after sectioning the final product.

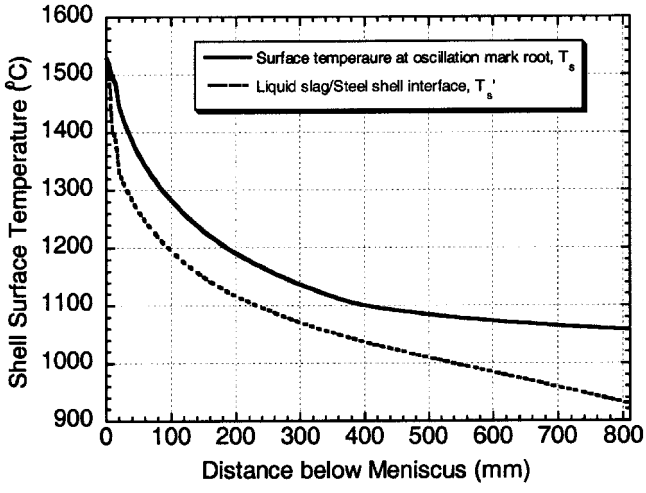


Fig. 17—Predicted shell surface temperature.

**Table III. Input Conditions for Submold Calibration (China Steel Case)**

| | | |
|---|---|---|
| Carbon content, C pct | 0.45 | pct |
| Mold thickness at top (including water channel) | 51 | mm |
| Initial cooling water temperature, $T_{water}$ | 35 | °C |
| Water channel geometry, $d_{ch} \times w_{ch} \times L_{ch}$ | $25 \times 5 \times 28$ | $mm^3$ |
| Cooling water velocity, $V_{water}$ | 7.62 | m/s |
| Casting speed, $V_c$ | 0.55 | m/min |
| Pour temperature, $T_{pour}$ | 1510 | °C |
| Slab geometry, $W \times N$ | $1560 \times 270$ | mm × mm |
| Nozzle submergence Depth, $d_{nozzle}$ | 200 | mm |
| Working mold length, $Z_{mold}$ | 600 | mm |
| Mold oscillation frequency | 120 | cpm |
| Oscillation stroke | 4 | mm |
| Cooling water temperature in spray zones, $T_{spray}$ | 35 | °C |
| Spray length of spray zone nozzle, $L_{spray}$ | 0.05 | m |
| Spray zone roll contact angle | 7 | deg |

Internal temperature histories measured at three places beneath the surface are included in Figure 18. Both surface thermocouples needed about 500 mm to heat to their surrounding shell temperatures and later suffered from internal debonding, so their results are reliable only between 500 and 3000 mm. The centerline thermocouple needed almost 2 m to heat, and appears to be accurate within 10 °C. Both the internal temperatures and the amplitude of their wiggles are roughly matched, indicating the degree of calibration. Temperature fluctuations at the thermocouple location are quite small, compared with the surface, which varies over 100 °C over a single roll pitch. Near the top of the caster, the greatest surface-temperature drop occurs beneath each spray jet, while a tiny dip occurs at each small region of direct contact with a support roll. Lower in the caster, the relative size of the dips becomes closer, with deep sharp drops caused by the high local heat-extraction rate during roll contact under high ferrostatic pressure.

Optical pyrometers are also useful for model calibration,[61] but are adversely affected by intermittent changes in surface-scale emissivity and steam density from evaporating spray water, so are most accurate when located below the spray chamber. Attaching thermocouples directly to the strand surface is another difficult experimental method that can be used for model calibration.[19]

## VI. SAMPLE APPLICATIONS

The calibrated model has many applications for both design and operation of continuous casting machines. First, it can help to investigate the effect of various process conditions on the fundamentals of mold heat transfer. Most parameters, such as oscillation practice, powder type, casting speed, and steel grade, affect heat transfer in several different ways, which can only be isolated and quantified independently using a model.

The model can make predictions of potential quality problems, which have more relevance in practice than simple heat transfer. For example, a warning of possible boiling in the cooling-water channels is issued when the mold surface temperature exceeds the pressure-dependent water boiling temperature. The model is currently being extended to make other warnings such as breakout danger from excessive shell

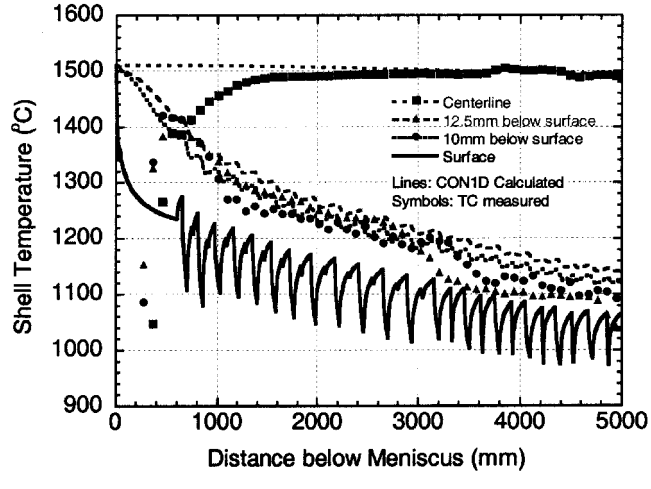


Fig. 18—Shell temperature (China Steel Case).

**Table IV. Spray Zone Variables (China Steel Case)**

| Zone | Zone Starts at (mm) | Roll in Zone (mm) | Roll Radius (mm) | Water Flow Rate (L/min/row) | Spray Width (m) | $f_{roll}$ |
|---|---|---|---|---|---|---|
| 1 | 600.0 | 2 | 70 | 27.5 | 1.3 | 0.05 |
| 2 | 906.9 | 5 | 70 | 14.86 | 1.2 | 0.05 |
| 3 | 1840.8 | 5 | 100 | 14.86 | 1.2 | 0.05 |
| 4 | 3034.3 | 5 | 125 | 11.84 | 1.2 | 0.2 |
| 5 | 4520.5 | 10 | 150 | 8.8 | 1.2 | 0.2 |
| 6 | 7977.9 | 10 | 175 | 7.15 | 1.2 | 0.2 |
| 7 | 11883.1 | 11 | 210 | 2.5 | 1.56 | 0.2 |
| 8 | 17050.7 | 18 | 240 | 0.0 | 1.56 | 0.2 |
| | 26440.7 | end of last spray zone | | | | |

**Table V. Parametric Study Conditions**

| Case | Casting Speed $V_c$ (m/min) | Oscillation Frequency (cpm) | Total Consumption Rate $Q_{slag}$ (kg/m$^2$) | Lubrication Consumption Rate $Q_{lub}$ (kg/m$^2$) | Oscil0 lation Mark Size $d_{mark} \times w_{mark}$ (mm$^2$) |
|---|---|---|---|---|---|
| 1 | 1.07 | 84 | 0.60 | 0.4 | 0.45 × 4.5 |
| 2 | 1.07 | 84 | 0.56 | 0.36 | 0.45 × 4.5 |
| 3 | 1.25 | 98 | 0.56 | 0.4 | 0.4 × 4.0 |

thinning at the mold exit, solid slag-layer fracture from excessive mold friction and the accompanying heat-flux variations, and crack formation. Finally, the model should predict optimum casting conditions to avoid problems, whenever possible. Initial features of the model toward this goal include a prediction of ideal mold taper. Together with other resources, CON1D is a powerful tool to investigate the cause and prevention of quality problems and to investigate potential design and operation improvements prior to costly experimental implementation.

### A. *Parametric Studies: Effect of Casting Speed*

As an example to illustrate the use of the model to understand fundamental phenomena in the mold, simulations were performed to investigate just two of the many interdependent parameters: casting speed and mold powder consumption. It is well known that increasing the casting speed causes changes to other parameters, such as decreased mold powder consumption rate and shallower oscillation marks. To investigate the effect of increasing casting speed in a typical real caster, the oscillation frequency was increased proportionally with speed, according to plant practice, and the oscillation-mark depth was decreased, such that the negative strip ratio and the lubrication consumption rate remained constant. The lubrication consumption rate ($Q_{lub}$) is a useful concept for comparing different powder consumption rates. It is introduced here as the rate of slag consumption, neglecting the slag carried in the oscillation marks:

$$Q_{lub} = Q_{slag} - Q_{osc} \quad [33]$$

Oscillation marks filled with slag and moving at the casting speed consume slag at the following rate ($Q_{osc}$):

$$Q_{osc} = \frac{0.5\rho_{slag} \times d_{mark} \times w_{mark}}{L_{pitch}} \quad [34]$$

Thus, the total consumption rate of slag ($Q_{slag}$) depends greatly on the oscillation-mark shape, while lubrication depends mainly on $Q_{lub}$, and mold heat transfer depends on both.

To investigate the effect of mold powder consumption rate, an intermediate case of a standard (low) casting speed with decreased consumption rate is also included. The three cases in this study are listed in Table V, with other conditions given in Table II.

Figure 19 presents the heat-flux profiles down the mold wide face, calculated for all three cases. Decreasing the powder consumption rate at a constant casting speed (case 2) is seen to increase heat flux in the top portion of the mold, relative to standard conditions (case 1). This is because the average thickness of the slag layers decreases, thus lowering the interfacial resistance. This effect diminishes with distance down the mold (as the importance of interfacial resistance to heat transfer decreases relative to that from increasing steel shell thickness).

The practical case of increasing the casting speed and simultaneously decreasing the total powder consumption rate and oscillation-mark depth (case 3) also increases heat flux toward the bottom of the mold. This is due to the lower thermal resistance of a thinner steel shell produced with less solidification time, which becomes increasingly important with distance down the mold. The net result of increasing the casting speed (comparing case 3 with case 1) is to increase heat flux almost uniformly down the mold. This is reflected in uniformly higher mold temperatures, as seen in the model predictions in Figure 20. This prediction also matches mold thermocouple measurements obtained for case 3 conditions, as included in Figure 20. The higher speed leads to a thinner steel shell and higher steel-surface temperature, so the liquid slag layer persists further down the mold, as shown in Figures 21 through 23, respectively. But, the higher heat flux for higher casting speed also lowers the shell-surface temperature, which partially cancels the effect of higher temperature due to the thinner shell. For these cases, the surface temperatures at the oscillation

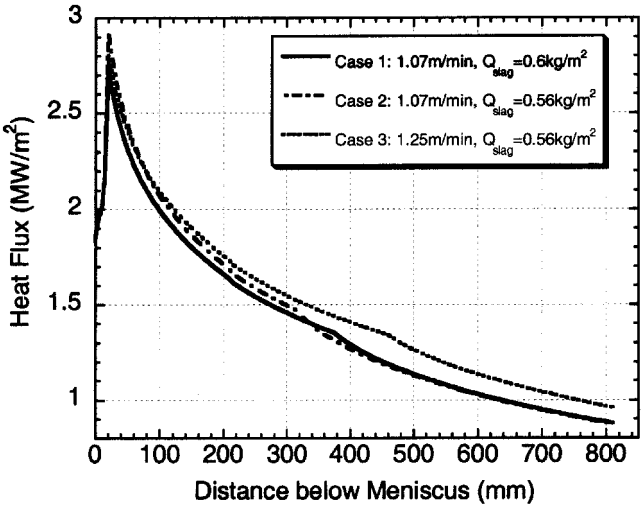


Fig. 19—Effect of casting speed and powder consumption on the heat flux profile.

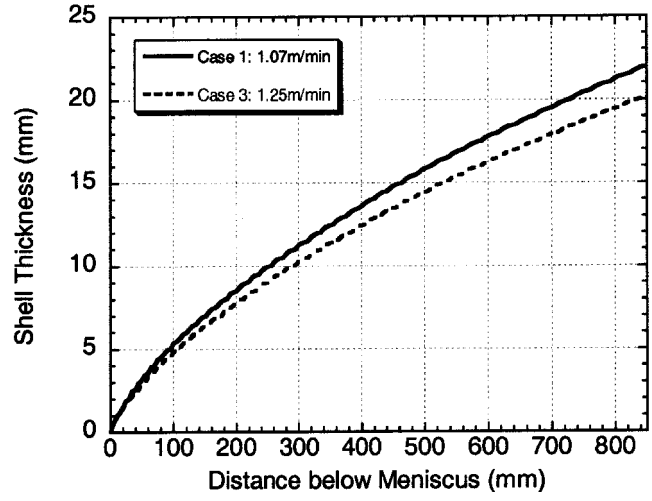


Fig. 21—Effect of casting speed on shell thickness.

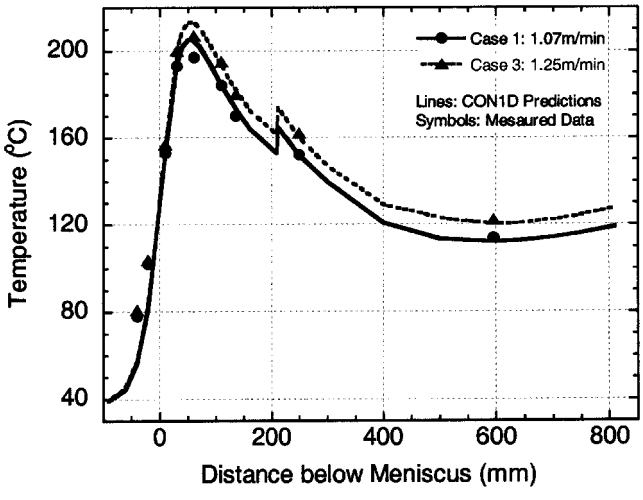


Fig. 20—Effect of casting speed on mold temperature.

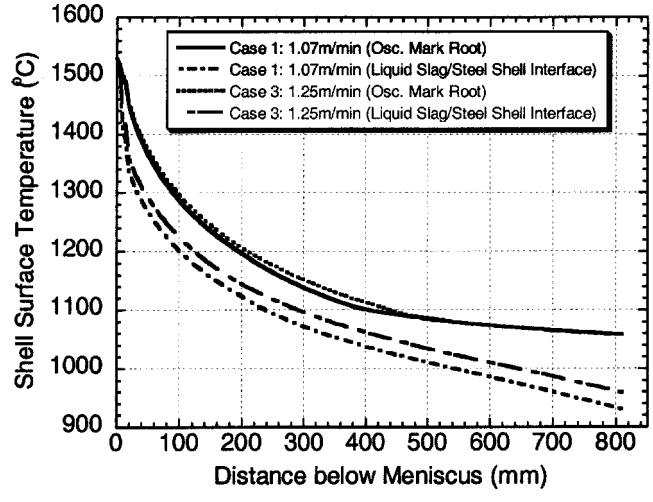


Fig. 22—Effect of casting speed on steel shell temperature.

mark's root near the mold exit are almost the same, as shown in Figures 22 and 24. Figure 24 compares the shell-temperature profiles at the mold exit.

The model is suited to many further fundamental parametric studies of this kind. For example, the steel grade affects the average oscillation-mark size, powder consumption rate, air-gap size due to thermal contraction (narrow face), and steel strength. Mold powder properties and oscillation practice have similar interdependent effects. The effect of oscillation-mark depth, for example, is quantified in a model application reported elsewhere.[73]

### B. *Boiling Prediction*

The model issues a warning that boiling is possible, if the mold cold-face temperature exceeds the boiling temperature for the given operating pressure in the cooling-water channels:[83]

$$\text{Boiling if: } T_{\text{cold}}\ (^{\circ}\text{C}) > 100\,(P\ (\text{MPa})/0.10135)^{0.27} \quad [35]$$

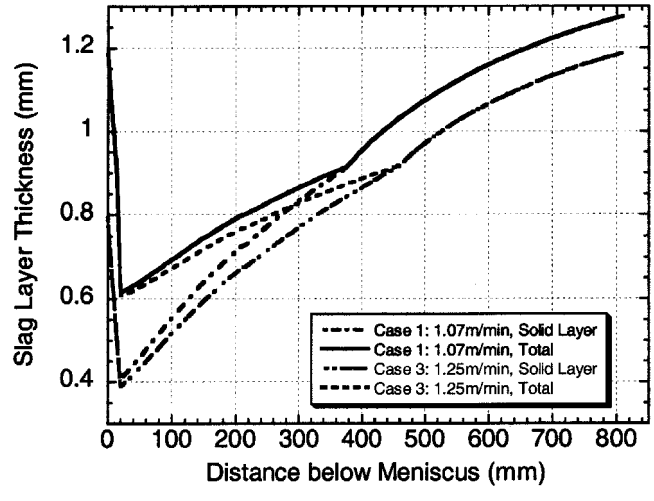


Fig. 23—Effect of casting speed on slag layer thickness.

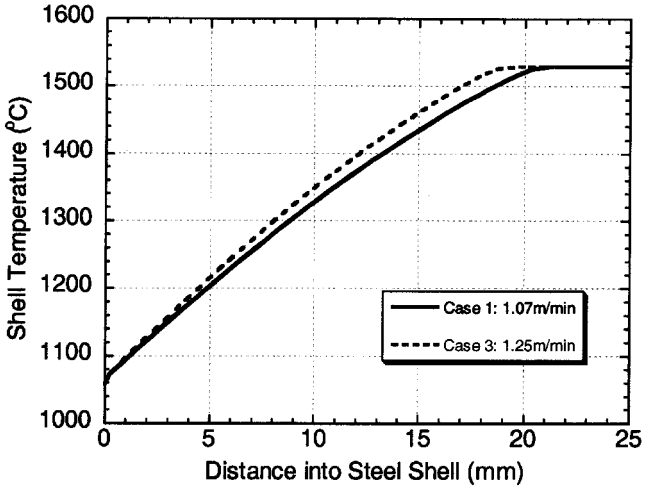


Fig. 24—Effect of casting speed on shell temperature profile at mold exit.

Boiling in the water channels changes the rate of heat removal and causes temperature fluctuations that together pose a serious potential quality problem. Figure 14 shows that boiling is, indeed, possible for the conditions investigated here. This is due to the 0.02-mm-thick layer of scale on the mold cold face near the meniscus, which raises the mold-face temperature ~ 70 °C. On the other hand, adding a 0.5-mm-thick protective Ni coating to the hot face is predicted to have only a minimal effect on heat flux and cold-face temperature. The CON1D model is ideal for quantifying effects such as these.

### C. *Breakout Analysis*

The model can be used to help understand how a breakout may have arisen. Sticker breakouts are easily identified by their characteristic effect on mold thermocouple histories. Other breakouts, such as those caused by inadequate taper, can be more difficult to identify. For example, the model could be used to determine whether a given narrow-face breakout was more likely caused by excessive superheat resulting from a clogged nozzle, or from an insufficient mold taper, causing an excessive gap. Either condition could produce a narrow-face shell that is too hot and thin to have the hot strength needed to avoid rupture. Further calibration may allow the model to accurately warn of a potential breakout when shell growth is predicted to fall below a critical value. Initial work toward this end is reported elsewhere.[30]

### D. *Lubrication Prediction*

The model is being extended to predict the consequences of interfacial heat transfer on mold friction and steel quality.[55] If the mold slag, which fills most of the gap, is allowed to cool completely below its crystallization temperature, then it becomes viscous and is less able to lubricate the strand. This may increase mold friction, cause the solid slag layer to fracture, and lead to transient temperature changes, making problems such as surface cracks more likely. Figure 16 suggests that this might occur below 400 mm, for the present conditions.

### E. *Crack-Formation Analysis*

As with previous continuous casting models, CON1D can be used to locate where defects are formed. For example, by accurately predicting the shell thickness existing the mold, the model can identify whether a subsurface crack formed in or below the mold. This can be difficult to tell, particularly near the narrow face, where shell growth is slower. Here, a crack forming below the mold might appear to have formed in the mold, without an accurate calculation of shell growth that incorporates superheat delivery. The model can also simulate phenomena below the mold, such as reheating of the shell surface, which can lead to surface cracks. Submold bulging and crack formation requires accurate temperature variation between rolls, so the model is useful for designing spray water-cooling systems.

### F. *Calculation of Ideal Mold Taper*

The narrow face of the mold should be tapered to match the shrinkage of the steel shell, which is cooling against the wide face. Previous work has determined that this shrinkage depends mainly on the surface temperature of the shell and the steel grade.[12] The model predicts an ideal average taper, by dividing the thermal strain ($\varepsilon$) by distance down the mold (instantaneous taper) or by the mold length (total taper per meter). Thermal-shrinkage strain is estimated here in two different ways; first, for $\varepsilon_{th1}$, by

$$\varepsilon_{th1} = \mathrm{TLE}(T_{\mathrm{sol}}) - \mathrm{TLE}(T_s) \quad [36]$$

Another method to calculate shrinkage was developed by Dippenaar *et al.*[34,84] The strain $\varepsilon_{th2}$ is computed by summing the average thermal linear expansion of the solid portion of the shell between each pair of consecutive time steps:

$$\varepsilon_{th2} = \sum_{t=0}^{t} \left( \left( \frac{1}{i} \right) \sum_{i=1}^{\text{solid nodes}} \left( \mathrm{TLE}(T_i^t) - \mathrm{TLE}(T_i^{t+\Delta t}) \right) \right) \quad [37]$$

Here, TLE is the thermal linear-expansion function for the given steel grade, calculated form weighted averages of the phases present.

For the sample cases, the higher speed causes a hotter shell with less shrinkage, shown in Figure 25, so it needs a slightly less-narrow-face mold taper. The shrinkage $\varepsilon_{th1}$, based on surface temperature only, is generally less than $\varepsilon_{th2}$ and is almost independent of casting speed, due to the cancellation effect discussed in Section VI–A. With a linear taper, the narrow-face shell attempts to shrink away from the upper portion of the mold, while it pushes against the lower portion of the mold. To match the shrinkage, it is clear that the taper should be increased high in the mold and decreased lower down. Mold distortion, viscoplastic creep of the steel, and other factors should also be taken into account when designing a nonlinear mold taper. These calculations require sophisticated thermal-stress models to calculate temperatures, stresses, and shrinkage, including the formation of an air gap near the corners, and its effect on heat flow across the mold/shell interface. The calibrated CON1D model is currently being used to provide calibrated heat-transfer data to these models to evaluate and improve taper optimization.

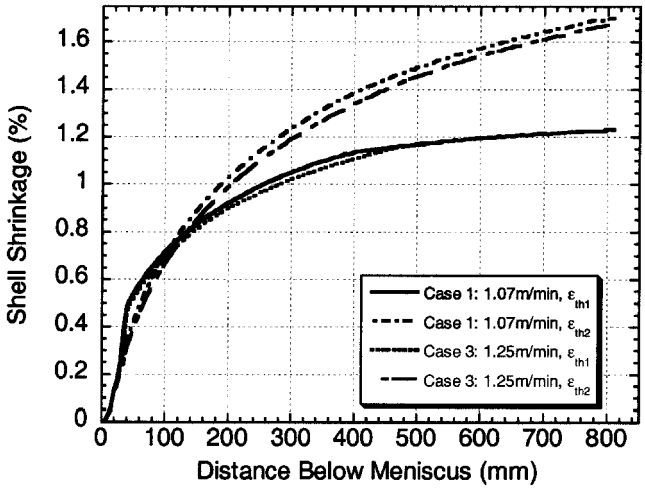


Fig. 25—Effect of casting speed on shell shrinkage.

### G. *Future Applications*

The model is based on conservation laws that must hold, regardless of the complex phenomena present in the caster. However, there are many more unknowns than equations. Thus, the model requires extensive calibration, which includes the values of many parameters not currently known. Preferably, some of the required input data should be predicted, such as powder consumption rate and oscillation-mark size.

Much further work is needed before the model can realize its full potential as a predictive tool for design, improvement, and control of continuous casting operations. For example, the model simulates only time-averaged behavior, while, in reality, many phenomena, especially involving the slag layer, vary greatly during each oscillation cycle. This requires a detailed, transient treatment. When and how the solid slag layer slides along the mold wall, the accompanying friction forces, and if and where the solid slag fractures are other important issues. Below the mold, fundamental measurements of spray-zone heat transfer are needed. This work will require advanced 3-D model-strand calculations, in addition to extensive calibration.

## VII. CONCLUSIONS

A simple but comprehensive heat-flow model of the continuous slab-casting mold, gap, and shell has been developed. It simulates 1-D solidification of the steel shell and features the dissipation of superheat, movement of the solid and liquid slag layers in the interfacial gap, and 2-D heat conduction within the copper mold wall. The model accounts for the effects of oscillation marks on both heat transfer and powder consumption. It also accounts for variations in water-slot geometry and steel grade. It is user friendly and runs quickly on a personal computer. It has been validated through numerical comparisons and calibrated with measurements on operating casters, including cooling water temperature rise, mold thermocouple temperatures, breakout shell thickness, slag layer thickness, and thermocouples embedded in the steel shell. In addition to heat transfer, the model predicts thickness of the solidified slag layers, ideal mold taper, and potential quality problems such as complete slag solidification and boiling in the water channels. It has many potential applications.

## ACKNOWLEDGMENTS

The authors thank former students Bryant Ho, Guowei Li, and Ying Shang for their work on early versions of the CON1D program and to the Continuous Casting Consortium, University of Illinois, and the National Science Foundation (Grant Nos. MSS-89567195 and DMI-01-15486) for funding, which made this work possible. Some 3-D computations for validation were performed at the National Center for Supercomputing Applications, UIUC. Special thanks go to Bill Emling and others, LTV Steel, and to Kuan-Ju Lin and others, China Steel, for collecting the operating data and experimental measurements used in model validation.

## NOMENCLATURE

| | |
|---|---|
| $C_p$ | specific heat (J/kgK) |
| $d$ | depth/thickness (m) |
| $d_b$ | diameter of the breakout hole (m) |
| $d_{osc}$ | volume-averaged oscillation-mark depth (mm) |
| $f_{roll}$ | fraction of heat flow per spray zone going to roll (—) |
| $f_s$ | solid steel fraction (—) |
| $f_v$ | empirical solid slag layer speed factor (—) |
| $g$ | gravity (9.81 m/s$^2$) |
| $h$ | heat-transfer coefficient (W/m$^2$K) |
| $h_{conv}$ | natural convection $h$ in spray zones (W/m$^2$K) |
| $h_{rad\_spray}$ | radiation $h$ in spray zones (W/m$^2$K) |
| $h_{rad}$ | radiation $h$ in slag layers (W/m$^2$K) |
| $k$ | thermal conductivity (W/mK) |
| $L$ | length (m) |
| $L_f$ | latent heat of steel (kJ/kg) |
| $L_{pitch}$ | distance between successive oscillation marks (m) |
| $n$ | exponent for temperature dependence of slag viscosity (—) |
| $N$ | slab thickness (m) |
| $Pr_{waterw}$ | Prandtl number of water at mold cold face temperature ($C_p\mu/k$) |
| $Q$ | average mold heat flux (kW/m$^2$) |
| $Q_{slag}$ | mold slag consumption (kg/m$^2$) |
| $Q_{water}$ | water flow rate in spray zones (L/m$^2$s) |
| $q_{int}$ | shell/mold interface heat flux (kW/m$^2$) |
| $q_{sh}$ | superheat flux (kW/m$^2$) |
| $Re_{waterf}$ | Reynolds number at average of mold cold face and cooling water temperatures ($DV\rho/\mu$) |
| $r_{contact}$ | slag/mold contact resistance (m$^2$K/W) |
| $t$ | time (s) |
| $t_d$ | drainage time (s) |
| $T$ | temperature (°C) |
| $T_{fsol}$ | mold slag solidification temperature (°C) |
| $T_{hotc}$ | mold copper hot face temperature (°C) |
| $T_{mold}$ | mold hot face temperature with coating (°C) |
| $T_{liq}$ | steel liquid temperature (°C) |
| $T_{sol}$ | steel solidus temperature (°C) |

| | |
|---|---|
| $T'_s$ | steel shell surface temperature (at oscillation mark root) (°C) |
| $T_s$ | liquid slag layer hot-side temperature (°C) |
| $\Delta T_{water}$ | cooling water temperature rise (°C) |
| TLE | thermal linear expansion (—) |
| $V_c$ | casting speed (m/s) |
| $w$ | width (m) |
| $W$ | slab width (m) |
| $x$ | shell thickness direction (m) |
| $z$ | casting-direction, distance below meniscus (m) |
| $Z_{mold}$ | working mold length (m) |
| $\alpha$ | thermal linear expansion coefficient ($K^{-1}$) |
| $\sigma$ | Stefan Boltzman constant ($5.67 \times 10^{-8}$ W/m$^2$K$^4$) |
| $\varepsilon$ | surface emissivities (—) |
| $\varepsilon_{th}$ | thermal strain of steel shell (pct) |
| $\rho$ | density (kg/m$^3$) |
| $\mu$ | viscosity (Pa s) |

*Subscripts*

| | |
|---|---|
| steel | steel slab |
| $\alpha$, $\delta$, $\gamma$, $l$ | $\alpha$-Fe, $\delta$-Fe, $\gamma$-Fe, liquid steel phases |
| mold | copper mold |
| coat | mold coating layer |
| water | cooling water (bulk) |
| ch | cooling water channel in mold |
| scale | scale layer in mold cooling channel |
| mark | oscillation mark |
| eff | effective oscillation mark (based on heat balance) |
| air | air gap |
| gap | shell/mold gap |
| slag | mold slag |
| solid, liquid | solid slag layer, liquid slag layer |
| spray | spray nozzle below mold |

## APPENDIX A

*FDM solution of steel solidification model*

Figure A1 shows the simulation domain in the solidifying steel, which is a slice through the liquid steel and solid shell and moves down at casting speed, $V_c$. Applying the boundary conditions,

$$\left.\frac{\partial T}{\partial x}\right|_{\text{centerline}} = 0 \qquad [A1]$$

$$k_{\text{steel}}(T_s)\left.\frac{\partial T}{\partial x}\right|_{\text{steel surface}} = -q_{\text{int}} \qquad [A2]$$

Equation [3] is solved at each time-step using the following explicit central finite difference discretization:

(1) Centerline liquid node (adiabatic boundary):

$$T_1^{\text{new}} = T_1 + \frac{2\Delta t \cdot k}{\Delta x^2 \rho Cp^*}(T_2 - T_1) \qquad [A3]$$

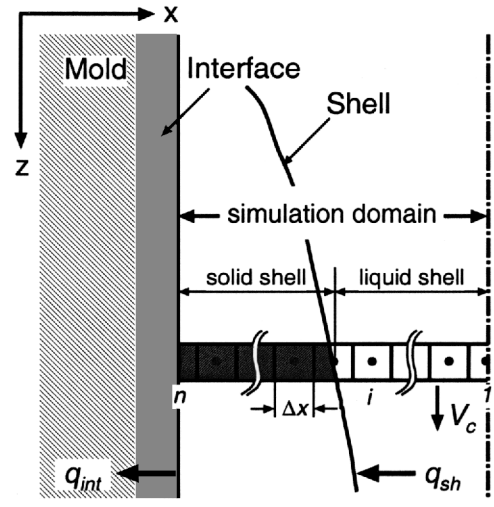


Fig. A.1—Simulation domain in shell.

(2) Interior nodes:

$$T_i^{\text{new}} = T_i + \frac{\Delta t \cdot k}{\Delta x^2 \rho Cp^*}(T_{i-1} - 2T_i + T_{i+1}) + \frac{\Delta t}{4\Delta x^2 \rho Cp^*}\frac{\partial k}{\partial T}(T_{i+1} - T_{i-1})^2 \qquad [A4]$$

(3) Shell surface node (with heat flux boundary):

$$T_n^{\text{new}} = T_n + \frac{2\Delta t \cdot k}{\Delta x^2 \rho Cp^*}(T_{n-1} - T_n) + \frac{\Delta t}{\rho Cp^*}\frac{\partial k}{\partial T}\left(\frac{q_{\text{int}}}{k}\right)^2 - \frac{2\Delta t \cdot q_{\text{int}}}{\Delta x \rho Cp^*} \qquad [A5]$$

The effect of superheat is included by adjusting Eq. [A4] for the first interior node with a temperature below the liquidus temperature:

$$T_i^{\text{new}} = T_i^{\text{new}} + \frac{\Delta t}{\rho Cp^* \, dx} q_{sh} \qquad [A6]$$

where $dx = \Delta x$ for interior nodes, and $dx = \Delta x/2$ for boundary nodes.

The preceding equations are solved at each time-step ($T_i^{\text{new}}$) based on properties evaluated at the previous step ($T_i$). This simple explicit scheme is usually acceptable because property changes are generally gradual with temperature (Figures 11 and 12). However, the effective specific heat has a sudden jump when temperature drops below the liquidus temperature. To improve accuracy, and allow a larger time-step, a postiteration correction is applied to each node after the time-step when it first drops below the liquidus temperature. Specifically, its temperature is increased to match the solid fraction that should have been achieved, based on converting the sensible heat extracted from that node into latent heat, according to the solid fraction curve $T(f_s)$ defined previously:

$$T_i^{\text{new}} = T\left(f_s = \frac{(T_{\text{liq}} - T_i^{\text{new}}) \cdot Cp^*(T_i)}{L_f}\right) \qquad [A7]$$

## APPENDIX B

*Mold thickness*

For a curved mold, the mold thickness, $d_{\text{mold}}$ varies with distance down the mold, which is calculated for the outer and inner radius mold faces separately:

$$d_{\text{mold}}^{\text{outer}} = d_{\text{moldo}}^{\text{outer}} + \sqrt{R_O^2 - \frac{1}{4}(Z_{\text{mold\_total}})^2} - \sqrt{R_o^2 - \frac{1}{4}(Z_{\text{mold\_total}})^2 - Z_{\text{mold\_total}}^2} \quad [B1]$$

$$d_{\text{mold}}^{\text{inner}} = d_{\text{moldo}}^{\text{inner}} - \sqrt{R_I^2 - \frac{1}{4}(Z_{\text{mold\_total}})^2} + \sqrt{R_I^2 - \frac{1}{4}(Z_{\text{mold\_total}})^2 - Z_{\text{mold\_total}}^2} \quad [B2]$$

where $d_{\text{moldo}}$ is the mold thickness at the top of the mold, $Z_{\text{mold\_total}}$ is the total mold length (sum of working mold length $Z_{\text{mold}}$ and distance of meniscus from top of the mold $Z_{\text{men}}$), and $R_O$, and $R_I$ are mold outer and inner radius of curvature, respectively.

## APPENDIX C

*Equilibrium partition coefficient, diffusion coefficient, and liquidus line slopes of the solute element*

The microsegregation model used here[68] evaluates dendrite arm spacing and phase fraction evolution as a function of cooling rate, $C_R$, and steel composition, $C_O$. Liquidus, solidus, and peritectic temperatures depend on steel composition as follows:

$$T_{\text{liq}} = T_{\text{pure}} - \sum_i m_i \cdot C_{0,i} \quad [C1]$$

$$T_{\text{sol}} = T_{\text{pure}} - \sum_i m_i \cdot C_{L,i}\left(C_{0,i}, k_i, D_i, C_R, f_s = 1\right) \quad [C2]$$

$$T^{\delta/\gamma} = T_{\text{pure}}^{\delta/\gamma} - \sum_i n_i \cdot k_i^{\delta/L} \cdot C_{L,i}^{\delta} \quad [C3]$$

Extended data needed for this model are listed in the following table and include the partition coefficients, $k$, and diffusion coefficients, $D$, for each phase, and the slopes of the equilibrium liquidus, $m$, and the slopes of $Ar_4$ lines, $n$, for the pseudobinary alloy of each element with iron. The results are not very sensitive to cooling rate, as the accompanying dendrite arm spacing change tends to compensate.

| Element | $k^{\delta/L}$ | $k^{\gamma/L}$ | $D^{\delta}$ (cm$^2$/s) | $D^{\gamma}$ (cm$^2$/s) | $m$ (°C/pct) | $n$ (°C/pct) |
|---|---|---|---|---|---|---|
| C | 0.19 | 0.34 | 0.0127 exp (−19,450/R$T$) | 0.0761 exp (−32,160/R$T$) | 78.0 | −1122 |
| Si | 0.77 | 0.52 | 8.0 exp (−59,500/R$T$) | 0.3 exp (−60,100/R$T$) | 7.6 | 60 |
| Mn | 0.76 | 0.78 | 0.76 exp (−53,640/R$T$) | 0.055 exp (−59,600/R$T$) | 4.9 | −12 |
| P | 0.23 | 0.13 | 2.9 exp (−55,000/R$T$) | 0.01 exp (−43,700/R$T$) | 34.4 | 140 |
| S | 0.05 | 0.035 | 4.56 exp (−51,300/R$T$) | 2.4 exp (−53,400/R$T$) | 38.0 | 160 |
| Cr | 0.95 | 0.86 | 2.4 exp (−57,310/R$T$) | 0.0012 exp (−52,340/R$T$) | 1.04 | 13.4 |
| Ni | 0.83 | 0.95 | 1.6 exp (−57,360/R$T$) | 0.34 exp (−67,490/R$T$) | 4.69 | −28.6 |
| Cu | 0.53 | 0.88 | 2.6 exp (−57,360/R$T$) | 0.7 exp (−68,350/R$T$) | 5.32 | −10.4 |
| Mo | 0.80 | 0.585 | 3.47 exp (−57,690/R$T$) | 0.068 exp (−59,000/R$T$) | 2.6 | 77.6 |
| Ti | 0.38 | 0.33 | 3.15 exp (−59,200/R$T$) | 0.15 exp (−59,980/R$T$) | 10.24 | 120.5 |
| V | 0.93 | 0.63 | 4.8 exp (−57,360/R$T$) | 0.284 exp (−61,900/R$T$) | 12.95 | 85.5 |
| Nb | 0.40 | 0.22 | 50.2 exp (−60,220/R$T$) | 0.83 exp (−63,690/R$T$) | 10.24 | 70.8 |
| W | 0.85 | 0.45 | 1.57 exp (−58,200/R$T$) | 0.13 exp (−57,300/R$T$) | 0.24 | 18.8 |
| N | 0.25 | 0.48 | 0.008 exp (−18,900/R$T$) | 0.91 exp (−40,270/R$T$) | 60.0 | — |

Note: R is the gas constant of 1.987 cal/mol K, and $T$ is the temperature in Kelvin.

## APPENDIX D

*Carbon steel thermal properties functions*

(1) Thermal conductivities

$$k = k_\alpha f_\alpha + k_\delta f_\delta + k_\gamma f_\gamma + k_l f_l$$

where

$$k_\alpha = (80.91 - 9.9269 \times 10^{-2}\, T + 4.613 \times 10^{-5}\, T^2)\,(1 - a_1\,(C\ \text{pct})^{a_2})$$

$$k_\delta = (20.14 - 9.313 \times 10^{-3}\, T)\,(1 - a_1 (C\ \text{pct})^{a_2}) \quad [D1]$$

$$k_\gamma = 21.6 - 8.35 \times 10^{-3}\, T$$

$$k_l = 39.0$$

$$a_1 = 0.425 - 4.385 \times 10^{-4}\, T$$

$$a_2 = 0.209 + 1.09 \times 10^{-3}\, T$$

(2) Specific heat

$$C_p = C_p^{\alpha} f_{\alpha} + C_p^{\delta} f_{\delta} + C_p^{\gamma} f_{\gamma} + C_p^{l} f_l$$

where

$$C_p^{\alpha} = \begin{cases} 504.8146 - 0.1311139T\,(\mathrm{K}) - 5.1875834 \times 10^{6} T\,(\mathrm{K})^{-2} \\ \quad + 4.486659 \times 10^{-4} T\,(\mathrm{K})^{2} & T\,(\mathrm{K}) \le 800 \\ -4720.324 + 4.583364T\,(\mathrm{K}) + 1.109483 \times 10^{9} T\,(\mathrm{K})^{-2} & 800 < T\,(\mathrm{K}) \le 1000 \\ -11501.07 + 12.476362T\,(\mathrm{K}) & 1000 < T\,(\mathrm{K}) \le 1042 \\ 34871.21 - 32.02658T\,(\mathrm{K}) & 1042 < T\,(\mathrm{K}) \le 1060 \\ -10068.18 + 5.98686T\,(\mathrm{K}) + 5.217657 \times 10^{9} T\,(\mathrm{K})^{-2} & 1060 < T\,(\mathrm{K}) \le 1184 \end{cases} \quad [D2]$$

$$C_p^{\delta} = 441.3942 + 0.17744236T\,(\mathrm{K})$$

$$C_p^{\gamma} = 429.8495 + 0.1497802T\,(\mathrm{K})$$

$$C_p^{l} = 824.6157$$

(3) Density used for thermal linear expansion calculation

$$\rho(T) = \rho_{\alpha} f_{\alpha} + \rho_{\delta} f_{\delta} + \rho_{\gamma} f_{\gamma} + \rho_{l} f_l$$

where

$$\rho_{\alpha} = 7880.76 - 0.3244T - 2.7461 \times 10^{-5} T^{2}$$

$$\rho_{\delta} = (8010.71 - 0.4724T) \cdot \left(1 + \frac{\text{C pct}}{100 - \text{C pct}}\right) \cdot (1 + 13.43 \times 10^{-3}\ \text{pct C})^{-3} \quad [D3]$$

$$\rho = (8105.91 - 0.5091T) \cdot \left(1 + \frac{\text{C pct}}{100 - \text{C pct}}\right) \cdot (1 + 8.317 \times 10^{-3}\ \text{pct C})^{-3}$$

$$\rho_{l} = 7965.98 - 0.619T$$

## REFERENCES


1. F.M. Najjar, B.G. Thomas, and D.E. Hershey: *Metall. Mater. Trans. B,* 1995, vol. 26B, pp. 749-65.
2. K.C. Mills: *Steel Technol. Int.,* 1994, pp. 161-66.
3. R.J. O'Malley: "An Examination of Mold Flux Film Structures and Mold Gap Behavior Using Mold Thermal Monitoring and Petrographic Analysis at Armco's Mansfield Operations", *Proc. METEC Congress 99*, (Dusseldorf, Germany, 13-15 June, 1999), Verein Deutscher Eisenhuttenleute, Dusseldorf, FRG, 1999.
4. R.J. O'Malley: *82nd Steelmaking Conf.,* Chicago, IL, 21-24 Mar., 1999, ISS/AIME, Warrendale, PA, 1999, vol. 82, pp. 13-33.
5. A. Yamauchi, K. Sorimachi, T. Sakuraya and T. Fujii: *Iron Steel Inst. Jen. Int.*, 1993, vol. 33 (1), pp. 140-47.
6. J. Cho, H. Shibata, T. Emi, and M. Suzuki: *Iron Steel Inst. Jpn. Int.*, 1998, vol. 38 (5), pp. 440-46.
7. M.S. Bhamra, M.G. Charlesworth, S. Wong, D. Sawyers-Villers, and A.W. Cramb: *54th Electric Furnace Conf.*, Dallas, TX, 9-12 Dec., 1996, ISS/AIME, Warrendale, PA, 1996, vol. 54, pp. 551-64.
8. C. Orrling, A.W. Cramb, A. Tilliander, and Y. Kashiwaya: *Iron Steelmaker,* 2000, vol. 27 (1), pp. 53-63.
9. Y. Kashiwaya, C.E. Cicutti, and A.W. Cramb: *Iron Steel Inst. Jpn. Int.*, 1998, vol. 38 (4), pp. 357-65.
10. B.G. Thomas, G. Li, A. Moitra, and D. Habing: *80th Steelmaking Conf.*, Chicago, IL, 1997, vol. 80, pp. 183-201.
11. X. Huang, B.G. Thomas, and F.M. Najjar: *Metall. Mater. Trans. B* 1992, vol. 23B, pp. 339-56.
12. A. Moitra and B.G. Thomas: *76th Steelmaking Conf.*, Dallas, TX, 28-31 Mar., 1993, ISS, Warrendale, PA, 1993, vol. 76, pp. 657-67.
13. B.G. Thomas: *1991 Steelmaking Conf.*, ISS, Warrendale, PA, 1991, pp. 69-82.
14. B.G. Thomas and L. Zhang: *Iron Steel Inst. Jpn. Int.* 2001, vol. 41 (10), pp. 1181-93.
15. B.G. Thomas: *Metall. Mater. Trans. B*, 2002, vol. 33B, pp. 795-812.
16. E.A. Mizikar: *Trans. TMS-AIME* 1967, vol. 239 (11), pp. 1747-58.
17. J.E. Lait, J.K. Brimacombe, and F. Weinberg: *Ironmaking and Steelmaking*, 1974, vol. 1 (2), pp. 90-97.
18. E.A. Upton, T.R.S. Rao, P.H. Dauby, and R.C. Knechtges: *Iron Steelmaker*, 1988, vol. 15 (5), pp. 51-57.
19. R. Davies, N. Blake, and P. Campbell: *4th Int. Conf. Continuous Casting, Preprints, Vol. 2*, Brussels, Belgium, 17-19 May, 1988, VS, Dusseldorf, FRG, 1988, vol. 2, pp. 645-54.
20. R.B. Mahapatra, J.K. Brimacombe, I.V. Samarasekera, N. Walker, E.A. Paterson, and J.D. Young: *Metall. Trans. B*, 1991, vol. 22B, pp. 861-74.
21. J.K. Brimacombe: *Can. Metall. Q.*, 1976, vol. 15 (2), pp. 163-75.
22. M.R. Aboutalebi, R.I.L. Guthrie, and M. Hasan: *Steel Res.*, 1994, vol. 65 (6), pp. 225-33.
23. F. Wimmer, H. Thone, and B. Lindorfer: *Berg. Huttenmannische Monatshefte*, 1996, vol. 141 (5), pp. 185-91.
24. H. Nam, H.S. Park, and J.K. Yoon: *Iron Steel Inst. Jpn. Int.*, 2000, vol. 40 (9), pp. 886-92.
25. S.K. Choudhary and D. Mazumdar: *Iron Steel Inst. Jpn. Int.*, 1994, vol. 34 (7), pp. 584-92.
26. B.G. Thomas, R.J. O'Malley, T. Shi, Y. Meng, D. Creech, and D. Stone: *Modeling of Casting, Welding and Advanced Solidification Process IX*, Aachen, Germany, 20-25 Aug., 2000, TMS, Warrendale, PA, 2000, pp. 769-76.
27. J.E. Lee, T.J. Yeo, K.H. Oh, J.K. Yoon, and U.S. Yoon: *Metall. Mater. Trans. A*, 2000, vol. 31A, pp. 225-37.
28. C. Ohler, H.J. Odenthal, H. Pfeifer, and I. Lemanowicz: *Stahl Eisen.*, 2002, vol. 122 (3), pp. 55-63.
29. B.G. Thomas, W.R. Storkman, and A. Moitra: *IISC 6th Int. Iron and Steel Congr.*, Nagoya, Japan, 21-26 Oct., 1990, ISIJ, Tokyo, Japan, 1990, vol 3, Steelmaking I, pp. 348-55.
30. C. Li and B.G. Thomas: *Brimacombe Memorial Symp.*, Vancouver, BC, Canada, 1-4 Oct., 2000, CIMMP, Montreal, PQ, Canada, 2000, pp. 595-611.

31. B.G. Thomas, A. Moitra, and R. McDavid: *Iron Steelmarker*, 1996, vol. 23 (4), pp. 57-70.
32. J.K. Park, I.V. Samarasekera, B.G. Thomas, and U.S. Yoon: *83rd Steelmaking Conf.*, Pittsburgh, PA, 26-29 Mar., 2000, ISS/AIME, Warrendale, PA, 2000, vol. 83, pp. 9-21.
33. C.A.M. Pinheiro, I.V. Samarasekera, and B.N. Walker: *Ironmaking and Steelmaking*, 2000, vol. 27 (1), pp. 37-54.
34. S. Chandra, J.K. Brimacombe, and I.V. Samarasekera: *Ironmaking and Steelmaking*, 1993, vol. 20 (2), pp. 104-12.
35. F. Wimmer, H. Thone, and B. Lindorfer: *Int. Conf. on Modelling and Simulation in Metallurgical Engineering and Materials Science*, Beijing, China, 11-13 June, 1996, *Metall. Industry Press*, Beijing, China, 1996, pp. 366-71.
36. N. Tiedje and E.W. Langer: *Scand. J. Metall.*, 1992, vol. 21 (5), pp. 211-17.
37. R. Bommaraju and E. Saad: *73th Steelmaking Conf.*, Detroit, MI, 25-28, Mar., 1990, ISS, Warrendale, PA, 1990, vol. 73, pp. 281-96.
38. J.A. DiLellio and G.W. Young: *Metall. Mater. Trans. B* 1995, vol. 26B, pp. 1225-1441.
39. J.F. Chavez, A. Celaya, M.A. Barron, and R.D. Morales: *79th Conf. of the Steelmaking Division of the Iron and Steel Society*, Pittsburgh, PA, 24-27 Mar., 1996, ISS/AIME, Warrendale, PA, 1996, vol. 79, pp. 321-29.
40. G.J.W. Kor: *Continuous Casting of Steel, 2nd Process Technology Conf.*, Chicago, II, 23-25 Feb., 1981, ISS/AIME, Warrendale, PA, 1981, vol. 2, pp. 124-32.
41. K. Nakajima: *Curr. Adv. Mater. Processing* 1992, vol. 5 (4), pp. 1221-24.
42. T. Cimarelli: *Metal Italiana*, 1997, vol. 89 (9), pp. 31-37.
43. D.R. Bland: *IMA J. Appl Math.*, 1984, vol. 32, pp. 89-112.
44. K. Harste: Ph.D. Dissertation, Technical University of Clausthal, Clausthal, 1989.
45. R.D. Pehlke, A. Jeyarajan, and H. Wada: Report No. NSFMEA82028, University of Michigan, Ann Arbor, MI, 1982.
46. H. Shibata, K. Kondo, and M. Suzuki: *Iron Steel Inst. Jpn. Int.*, 1996, vol. 35, Suppl., pp. S179-S182.
47. B. Ho: Master's Thesis, University of Chicago, Urbana, IL, 1992.
48. K. Ichikawa, A. Morita, and Y. Kawabe: *Shinagawa Techn. Rep.*, 1993, vol. 36, pp. 99-107.
49. K. Watanabe, M. Suzuki, K. Murakami, H. Kondo, A. Miyamoto, and T. Shiomi: *NKK Techn. Rev.*, 1997, vol. 77, pp. 20-26.
50. R. Taylor and K.C. Mills: *Ironmaking and Steelmaking*, 1988, vol. 15 (4), pp. 187-94.
51. A.C. Mikrovas, S.A. Argyropoulos, and I.D. Sommerville: *Iron Steelmaker*, 1991, vol. 18 (12), pp. 51-61.
52. M.S. Jenkins: in *Continuous Casting*, vol. 9, *Initial Solidification and Strand Surface Quality of Peritectic Steels*, ISS-AIME, Warrendale, PA, 1997, pp. 239-44.
53. M.D. Lanyi and C.J. Rosa: *Metall. Trans. B*, 1981, vol. 12B (2), pp. 287-98.
54. D. Larson: *Ind. Heating*, 1986, vol. 53 (4), pp. 16-17.
55. Y. Meng and B.G. Thomas: *Metall. Mater. Trans. B*, 2003, vol. 34B, pp. 707-25.
56. H.S. Carslaw and J.C. Jaeger: *Conduction of Heat in Solids*, 2nd ed., Oxford University Press, Oxford, United Kingdom, 1986.
57. L.C. Burmesiter: *Convective Heat Transfer*, 2nd ed., Wiley, New York, NY, 1993, p. 484.
58. C.A. Sleicher and M.W. Rouse: *Int. J. Heat Mass Transfer*, 1975, vol. 18 (5), pp. 677-83.
59. F.W. Dittus and L.M.K. Boelter: *Univ. Calif. Publ. Eng.*, 1930, No. 2, pp. 443-61.
60. M.M. Langeneckert: Master's Thesis, University of Illinois, Urbana, IL, 2001.
61. J.K. Brimacombe, P.K. Agarwal, S. Hibbins, B. Prabhaker, and L.A. Baptista: *Continuous Casting*, ISS/AIME, Warrendale, PA, 1984, vol. 2, pp. 109-23.
62. T. Nozaki: *Iron Steel Inst. Jpn. Trans.*, 1978, vol. 18, pp. 330-38.
63. R.A. Hardin, H. Shen, and C. Beckermann: *Modelling of Casting, Welding and Advanced Solidification Processes IX*, 20-25 Aug., 2000, TMS, Warrendale, PA, 2000.
64. R.D. Pehlke: *Enginneering Summer Conf.: Continuous Casting of Steel*, Univ. of Michigan, Ann Arbor, MI, 1980, Section VII, pp. 1-17.
65. V.R. Voller, C.R. Swaminathan, and B.G. Thomas: *Int. J. Num. Methods in Eng.*, 1990, vol. 30, pp. 875-98.
66. B.G. Thomas and Y. Meng: *CON1D Users Manual*, University of Illinois, Urbana, IL, 2002.
67. A. Kagawa and T. Okamoto: *Mater. Sci. Technol.*, 1986, vol. 2 (10), pp. 997-1008.
68. Y.M. Won and B.G. Thomas: *Metall. Mater. Trans. A*, 2001, vol. 32A, pp. 1755-67.
69. G. Li: Ph.D. Thesis, University of Illinois, Urbana, IL, 1996.
70. B.G. Thomas and T. Morthland: "3-*D Heat Transfer Analysis of Columbus Slab Casting Mold*," CCC Report 2001, Univ. of Ill., Urbana, IL.
71. B.G. Thomas, B. Ho, and G. Li: *Alex McLean Symp.: Process Fundamentals, Liquid Metal Processing for Cleanliness, Novel and Conventional Casting, and Novel Process Technologies*, Toronto, ON, Canada, 1998, pp. 177-93.
72. D.R. Poirier and G.H. Geiger: *Transport Phenomena in Materials Processing*, TMS, Warrendaler, PA, 1994, p. 339.
73. B.G. Thomas, D. Lui, and B. Ho: *Sensors and Modeling in Materials Processing: Techniques and Applications*, Orlando, FL, 1997, pp. 117-42.
74. M.M. Collur: "*Use of CONID Model to Determine if the Casting Speed can be Increased for Chrome-Nickel Grades at 8-3 Caster*," Report, Allegheny Ludlum Corporation Technical Center, Brackenridge, PA, 1996.
75. J. Paidipati, B. Sharos, C. Slayton, and J. Wood: Report No. 6: ME280 Final Report, University of Illinois, Urbana, IL, 2002.
76. J.K. Park: Ph.D. Thesis, University of British Columbia, Vancouver, BC, Canada, 2002.
77. B.G. Thomas: *79th Conf. of the Steelmaking Division of the Iron and Steel Society*, Pittsburgh, PA, 24-27 Mar., 1996, ISS/AIME, Warrendale, PA, 1996, pp. 519-31.
78. J.K. Park, B.G. Thomas, and I.V. Samarasekera: *Ironmaking and Steelmaking*, 2002, vol. 29(5), pp. 359-75.
79. R. Sobolewski, S.C. Sander, J.G. Kuczma, and A.J. Rumler: *Steelmaking Conf. Proc.*, Detroit, MI, 1990, vol. 73, pp. 275-80.
80. I.V. Samarasekera and J.K. Brimacombe: *Ironmaking and Steelmaking*, 1982, vol. 9 (1), pp. 1-15.
81. A. Moitra: Ph.D Thesis, University of Illinois, Urbana-Champaign, IL, 1993.
82. G.D. Lawson, S.C. Sander, W.H. Emling, A. Moritra, and B.G. Thomas: *77th Steelmaking Conf.*, Chicago, IL, 20-23 Mar., 1994, ISS/AIME, Warrendale, PA, 1994, vol. 77, pp. 329-36.
83. *CRC Handbook of Chemistry and Physics*, R.C. Weast, ed., Chemical Rubber Co., Cleveland, OH, 1971.
84. R.J. Dippenaar, I.V. Samarasekera, and J.K. Brimacombe: *ISS Trans.*, 1986, No. 7, pp. 31-43.
85. B.G. Thomas, M. Langeneckert, L. Castella, M. Dziuba, G.D. Gresia and W. Balante: *Ironmaking and Steelmaking*, 2003, vol. 30 (3), pp. 1-5.